

Annual Review of Astronomy and Astrophysics
**Stellar Dynamics and Stellar
 Phenomena Near a Massive
 Black Hole**

Tal Alexander

Department of Particle Physics and Astrophysics, Weizmann Institute of Science, Rehovot
 76100, Israel; email: tal.alexander@weizmann.ac.il

Annu. Rev. Astron. Astrophys. 2017. 55:17–57

First published as a Review in Advance on June 2,
 2017

The *Annual Review of Astronomy and Astrophysics* is
 online at astro.annualreviews.org

<https://doi.org/10.1146/annurev-astro-091916-055306>

Copyright © 2017 by Annual Reviews.
 All rights reserved

Keywords

Galactic dynamics, stellar kinematics, Galactic Center, gravitational waves,
 tidal disruption

Abstract

Most galactic nuclei harbor a massive black hole (MBH), whose birth and evolution are closely linked to those of its host galaxy. The unique conditions near the MBH—high velocity and density in the steep potential of a massive singular relativistic object—lead to unusual modes of stellar birth, evolution, dynamics, and death. A complex network of dynamical mechanisms, operating on multiple timescales, deflects stars to orbits that intercept the MBH. Such close encounters lead to energetic interactions with observable signatures and consequences for the evolution of the MBH and its stellar environment. Galactic nuclei are astrophysical laboratories that test and challenge our understanding of MBH formation, strong gravity, stellar dynamics, and stellar physics. I review from a theoretical perspective the wide range of stellar phenomena that occur near MBHs, focusing on the role of stellar dynamics near an isolated MBH in a relaxed stellar cusp.



**ANNUAL
REVIEWS Further**

Click here to view this article's
 online features:

- Download figures as PPT slides
- Navigate linked references
- Download citations
- Explore related articles
- Search keywords

Contents

1. INTRODUCTION AND OUTLINE	18
1.1. Motivation	18
1.2. MBHs and Their Stellar Hosts	19
1.3. Unique Properties Inside the MBH Radius of Influence	21
1.4. The Special Role of the Galactic MBH Sgr A*	22
1.5. Scope of This Review	25
2. DYNAMICAL RELAXATION NEAR AN MBH	25
2.1. Noncoherent Relaxation	27
2.2. Resonant Relaxation (Coherent Relaxation)	31
2.3. A General Framework for Describing Relaxation	32
3. DYNAMICS OF CLOSE MBH–STAR ENCOUNTERS	33
3.1. The Newtonian Loss Cone	33
3.2. The Relativistic Loss Cone	37
3.3. Noncollisional Loss-Cone Refilling	41
4. TIDAL INTERACTIONS BETWEEN STARS AND AN MBH	41
4.1. Classification of Tidal Disruptions	41
4.2. Stellar Disruption	42
4.3. Near Misses	44
4.4. Three-Body Exchange Interactions	45
5. RELATIVISTIC INTERACTIONS WITH AN MBH	47
5.1. Gravitational Waves from Extreme Mass–Ratio Inspirals	48
5.2. Stars and Pulsars on Relativistic Orbits in the Galactic Center	48
6. STAR–STAR COLLISIONS NEAR AN MBH	49
6.1. Collisional Destruction and Mergers	49
6.2. Collisions Involving Binaries	50
7. STARS AND CIRCUMNUCLEAR ACCRETION DISKS	51
7.1. Hydrodynamical Star–Disk Interactions	51
7.2. Gravitational Star–Disk Interactions (Disk Warping)	52
7.3. Disk Fragmentation and Star Formation	52
8. FUTURE PROSPECTS	52

1. INTRODUCTION AND OUTLINE

1.1. Motivation

Massive black holes (MBHs) with masses $M_{\bullet} \sim 10^6\text{--}10^{10} M_{\odot}$ lie in the nuclei of most galaxies (see the review by Graham 2016). This conclusion follows from the cosmic statistics of active galactic nuclei (AGNs), which are powered by an MBH (see review by Netzer 2015), from the analysis of gas and stellar dynamics observed in well-resolved galactic nuclei in the nearby Universe (Ferrarese & Merritt 2000, Gebhardt et al. 2000, Kormendy & Ho 2013), from the rare edge-on maser emitting circumnuclear accretion disks that allow precise dynamical measurements (Miyoshi et al. 1995), from comparing the mean mass density in the cosmic UV background (assumed to be generated by AGNs) to the space density of galaxies (Soltan 1982, Yu & Tremaine 2002), and finally, from detailed studies of the faint accretion emission and the stellar motions around Sgr A*, the MBH

MBH: massive black hole

AGN: active galactic nucleus

closest to us in the center of the Milky Way (see reviews by Alexander 2005, Genzel et al. 2010), which provide the strongest empirical evidence for the existence of an MBH.

The ubiquity of MBHs and of their phases of massive outflows and huge radiative output, which can outshine their host galaxy, places MBHs at the crossroads of many phenomena and processes in the realms of cosmology, astrophysics, and strong gravity, both as active agents and as probes.

MBHs in galactic nuclei are embedded in a dense stellar environment. This is observed in the Milky Way and in nearby galaxies (e.g., Lauer et al. 1998, Fritz et al. 2016), and is predicted theoretically for isolated galactic nuclei (Bahcall & Wolf 1977, Young 1977). Of the wide range of complex processes associated with MBHs and their close environments, stellar phenomena are substantially more tractable for analysis and modeling. This is because in many cases the stars can be treated as point masses, which are affected only by gravity, and are free from the microphysical uncertainties of nongravitational forces that may dominate gas-phase dynamics, such as radiation pressure, magnetic fields, and hydrodynamic turbulence. The very large ratio of the mass of a star to that of the MBH allows the problem to be simplified even further by treating the stars as test masses on intermediate distance and timescales in which the stars are deep enough in the MBHs potential so that star–star gravitational interactions are negligible but not so close to the MBH that tidal effects are important. In that limit, where each star separately can be approximated as forming a two-body system with the MBH, atomic physics can provide useful analogies and tools for dealing with three- and four-body interactions (see the review by Alexander 2005). For many purposes the much simpler Newtonian treatment of the dynamics suffices, and general relativity (GR) effects can be omitted. Even when the finite stellar mass, size, and life span can no longer be neglected, and stellar evolution becomes relevant, the uncertainties in the analysis and modeling can be reduced by drawing on the well-developed theoretical understanding of stellar structure and evolution and on the large body of detailed stellar observations away from galactic nuclei, in the low-density field, and in dense stellar clusters.

The presence of an MBH in a high-density stellar cluster offers opportunities to test theories of stellar structure and evolution. Dynamics near MBHs with masses $<10^8 M_\odot$ are collisional (Alexander 2011, Bar-Or et al. 2013). Stellar velocities close to the MBH exceed the escape velocity from the stellar surface (i.e., the kinetic energy in a star–star collision exceeds the stellar binding energy), and collision rates rise to a level where many of the stars suffer strong encounters (e.g., Alexander & Kumar 2001). Likewise, tidal encounters with the MBH can substantially perturb the internal stellar structure (Alexander & Livio 2001, Manukian et al. 2013). Such galactic nuclei are effectively stellar colliders that probe the physics of stellar interiors by smashing stars energetically against each other and against the MBH.

1.2. MBHs and Their Stellar Hosts

The MBH dominates the gravitational potential inside its radius of influence, r_h , which can be estimated by equating the potential of the MBH, were it not surrounded by stars, to the potential of the galactic nucleus, in the absence of an MBH, $-GM_\bullet/r_h = \phi_\star(r_h)$. When ϕ_\star is approximated as a singular isothermal distribution (stellar mass density $\rho_\star = \sigma^2/2\pi Gr^2$), whose potential has a constant velocity dispersion σ , the radius of influence is $r_h = GM_\bullet/\sigma^2$, and the total mass in stars within r_h is $\mathcal{O}(M_\bullet)$. This is a useful approximation for galactic nuclei, because typically, stellar dynamical processes drive the stellar distribution near an isolated MBH to a power-law cusp,¹ not much different from an isothermal sphere (Section 2).

¹This is quite unlike the case of a cluster with a dense core of mass M_c , size R_c , dispersion $\sigma_c^2 \sim GM_c/R_c$, and a (hypothetical) central intermediate-mass black hole (IMBH) with $M_\bullet \ll M_c$. There the total mass in stars within r_h is $\propto (M_\bullet/M_c)^2 M_\bullet \ll M_\bullet$ (e.g., Lasota et al. 2011).

BH: black hole
IMBH:
intermediate-mass
black hole

There are strong empirical correlations between the masses of MBHs and the spheroidal component of their host galaxies (the bulge in the case of spirals, or the entire galaxy in the case of ellipticals). The stellar velocity dispersion σ in the bulge (on length scale $\gg r_h$) correlates with the MBH mass as $M_\bullet = M_0(\sigma/\sigma_0)^\beta$, with $\beta \sim 4-5$ (Ferrarese & Merritt 2000, Gebhardt et al. 2000, McConnell et al. 2011) (the M_\bullet/σ relation). The MBH's mass scales with the bulge's mass M_b as $M_\bullet = \epsilon_\bullet M_b$, with $\epsilon_\bullet \sim (1-2) \times 10^{-3}$ (Magorrian et al. 1998, Häring & Rix 2004). These correlations with properties on scales well beyond the MBH's direct dynamical reach suggest a fundamental evolutionary link between MBHs and their host galaxies, which may be due to feedback by the powerful outflows in the MBH's AGN phase but whose exact nature is still unclear (see the review by King & Pounds 2015).

The presence of a dense central stellar cluster in a galactic nucleus does not necessarily imply the presence of an MBH. Nuclear stellar clusters with no detectable MBHs are observed in lower-mass galaxies ($\lesssim 10^{10} M_\odot$), whereas the nucleus of very massive galaxies ($\gtrsim 10^{12} M_\odot$) is completely dominated by the MBH. MBHs and nuclear stellar clusters often coexist in galaxies in the intermediate-mass range (Georgiev et al. 2016).

Conversely, the absence of a dense central stellar cusp² does not imply the absence of an MBH. Massive galaxies tend to have cored nuclei. The extrapolation back to the origin of the decreasing density profile outside the core supports the idea that $\mathcal{O}(M_\bullet)$ of stellar mass was removed from a previously existing cusp (Kormendy & Bender 2009, Thomas et al. 2014). A natural explanation is that past galactic mergers led to the formation of a tight MBH binary, which decayed dynamically and coalesced to form the present MBH by ejecting a stellar mass comparable with its own from the nucleus, leaving behind a lower-density stellar core (Begelman et al. 1980, Milosavljević et al. 2002).

AGN statistics imply that MBHs exist in all galaxy types (Kauffmann et al. 2003). Some are found at high redshifts of $z \gtrsim 7$, when the Universe was only $\lesssim 5\%$ of its present age, and yet they appear to be already very massive then, with $M_\bullet \gtrsim 10^9 M_\odot$ (e.g., Mortlock et al. 2011). This requires a very efficient formation process that allows MBHs to grow very fast, very soon after the Big Bang. Early stellar populations are implicated in some of the proposed scenarios for creating or rapidly growing an MBH seed that can jump-start the relatively slow process of growth by disk accretion (Volonteri 2012): Rapid stellar collisions of low-metallicity stars in very dense clusters can lead to the runaway formation of a very massive star by mergers, which retains most of its mass as it collapses directly into a black hole (BH) (Omukai et al. 2008, Devecchi & Volonteri 2009, Davies et al. 2011), or a stellar BH that is launched into a phase of supra-exponential accretion from the dense cold ISM of high- z protoclusters by the random gravitational perturbations of the other stars (Alexander & Natarajan 2014).

IMBHs, with masses between the $\mathcal{O}(10 M_\odot)$ scale of stellar BHs and the $\mathcal{O}(10^6 M_\odot)$ scale of the lightest detected MBHs, are expected to exist in dense stellar clusters. This is based on an extrapolation of the M_\bullet/σ relation to low masses, and it also follows from various formation scenarios, which either allow some IMBHs to form late, so they would not have had time to grow further, or else require special conditions, whose chance absence can stall the IMBH's growth. The continuing lack of firm evidence for IMBHs remains puzzling (see the review by Miller & Colbert 2004).

²A cusp is a density distribution that formally diverges at $r \rightarrow 0$, e.g., a power-law $n_\star \propto r^{-\alpha}$ with $\alpha > 0$. A cored density distribution flattens to a finite central density inside the core radius.

1.3. Unique Properties Inside the MBH Radius of Influence

MBHs in dynamically relaxed galactic nuclei are expected to be surrounded by a very dense stellar system. The singular character of MBHs and the extreme properties of their close environment make these systems unique physical laboratories.

GW: gravitational wave

AI: adiabatic invariance

1.3.1. A singular relativistic potential. The MBH's deep gravitational potential dominates over stellar gravity well inside r_h and imposes on the system its spherical symmetry (for a nonspinning Schwarzschild MBH) or axial symmetry (for a spinning Kerr MBH). Because the dynamical effects of the MBH spin fall rapidly with distance (above $r \gtrsim 10r_g$, where $r_g = GM_\bullet/c^2$ is the MBH's gravitational radius), the potential over $r_g \ll r < r_h$ is to leading order spherical irrespective of the MBH spin. This high degree of approximate symmetry limits orbital evolution around the MBH to nearly fixed Keplerian ellipses on nearly fixed planes. Poisson fluctuations away from spherical symmetry, due to the finite number of stars in the system, result in residual forces that exert coherent (resonant) torques on the orbits, leading to rapid angular momentum evolution (Rauch & Tremaine 1996; Section 2.2).

Secular relativistic dynamical effects, such as the advance of the angle of periastron (Schwarzschild precession), Lense–Thirring precession of the orbital plane around a spinning MBH, Bardeen–Petterson torques on an accretion disk (Bardeen & Petterson 1975), or orbital decay by the emission of gravitational waves (GWs), all fall rapidly with distance but can nevertheless have substantial effect over time even for mildly relativistic orbits (e.g., Levin & Beloborodov 2003). The strong coherent Newtonian torques and the relativistic effects are coupled. On the one hand, the coherent torques compete with the more subtle relativistic effects, making tests of strong gravity very challenging (Merritt et al. 2010). On the other hand, fast relativistic precession can suppress the coherent torquing by adiabatic invariance (AI), decoupling relativistic orbits from the perturbing background (Merritt et al. 2011, Bar-Or & Alexander 2014). In particular, this effect allows stellar BHs to inspiral unperturbed into MBHs by the emission of GWs (Hopman & Alexander 2006, Bar-Or & Alexander 2016; Section 3.2).

In marked contrast to the shallower potentials of dense clusters, the deep singular potential of the MBH allows the retention of a dense concentration of stellar BHs (Preto & Amaro-Seoane 2010), which accumulate close to the center owing to mass segregation (Section 2.1.4), and play an important role in the acceleration of dynamical processes there.

1.3.2. A strong tidal field. The diverging potential of the MBH allows the tidal force on any bound object (a star, a binary, a gas cloud) with mass M_\star and size R_\star , $F_t \sim GM_\bullet M_\star R_\star / r^3$, to exceed its self-gravity $F_s \sim GM_\star^2 / R_\star^2$ if the distance r from the MBH is small enough, $r < r_t \simeq (M_\bullet / M_\star)^{1/3} R_\star$. The object is then tidally disrupted, and its unbound fragments fly off on ballistic orbits. The tidal disruption condition can be stated alternatively in terms of the distance where the star's mean density falls below the density the MBH would have if its mass were spread over r_t , $\rho_\star = M_\star / R_\star^3 \leq M_\bullet / r_t^3$, or in terms of the distance where the crossing time of the tidal disruption zone falls below the star's dynamical time $\sqrt{r_t^3 / GM_\bullet} \leq \sqrt{R_\star^3 / GM_\star} = t_\star$.

The only limit on disruption by an MBH is set by the size of the event horizon $R_\bullet = x_\bullet r_g$ ($x_\bullet = 2$ for a nonspinning BH; generally $1 \leq x_\bullet \leq 9$, with $x_\bullet = 1$ for an equatorial co-rotating orbit around a maximally spinning Kerr BH, and $x_\bullet = 9$ for an equatorial counter-rotating orbit). When $r_t < R_\bullet$, the disruption is hidden and confined inside the event horizon, and a distant observer sees a direct plunge. Because $r_t / R_\bullet \propto \rho_\star^{-1/3} x_\bullet^{-1} M_\bullet^{-2/3}$, there exists for a star of given mean density ρ_\star a maximal MBH mass that allows tidal disruption outside of the event horizon; the higher the MBH spin, the larger is $\max M_\bullet$; for Solar type stars and a Schwarzschild MBH it is

WD: white dwarf

MS: main sequence

TDE: tidal disruption event

HVS: hypervelocity star

$\max M_{\bullet} \sim 10^8 M_{\odot}$ (see the review by Alexander 2012). The lower the MBH mass is, the denser the stars it can disrupt outside R_{\bullet} . An IMBH can tidally disrupt even a white dwarf (WD), (Luminet & Pichon 1989). Conversely, very dense low-mass main sequence (MS) stars ($\rho_{\star} \propto M_{\star}^{-11/4}$ for $M_{\star} \lesssim 1.5 M_{\odot}$, Schaller et al. 1992), can survive the MBH tidal field and inspiral by the emission of GWs (Freitag 2003).

Tidal disruption events (TDEs) by MBHs are expected to lead to short accretion flares, which can signal the presence of an otherwise quiescent MBH (Rees 1988), and probe both the accretion physics and the dynamics leading to the TDE (Section 4). The number of observed candidate TDEs is fast growing, and it is becoming clear that this class of variable sources has a much richer phenomenology than captured by the initial simplified models (Komossa 2015).

1.3.3. A high stellar density. The stellar density distribution around an isolated MBH, well inside r_h , is expected to rise sharply as an approximate power-law cusp $n_{\star} \propto r^{-\alpha}$ (Section 2.1.4). This occurs whether the system is formed adiabatically on a timescale shorter than the two-body relaxation time, in which case the power-law index depends on the initial conditions, for example, $\alpha = 3/2 - 5/2$ when the surrounding stellar system is isothermal (Young 1977), or whether the system is dynamically relaxed, in which case $\alpha = 7/4 - 5/2$, depending on the stellar mass function (Bahcall & Wolf 1977, Alexander & Hopman 2009, Keshet et al. 2009, Preto & Amaro-Seoane 2010). For lighter MBHs, the mean stellar density inside r_h can be as high as that of the cores of the densest globular clusters (Section 2.1); the local density rises rapidly toward the MBH and can reach densities that are a few orders of magnitude higher than anywhere else in the Universe. Because the rate of collisions per star scales with n_{\star} , destructive stellar collisions (e.g., Alexander 1999) and strong nondestructive tidal and grazing stellar encounters (Alexander & Kumar 2001) become dynamically important near the MBH and affect the stellar population there.

The high-density cusp can be destroyed, or prevented from forming, by external perturbations, such as galactic mergers that lead to the formation of an MBH binary, which slings out the stars inside its orbit as it decays (Begelman et al. 1980, Milosavljević & Merritt 2001, Merritt & Milosavljević 2005).

1.3.4. High orbital velocities. The singular potential of the MBH allows stars to approach the MBH up to the tidal disruption radius and reaches velocities of up to $v \sim \sqrt{2GM_{\bullet}/r_t} \sim \sqrt{2}(M_{\bullet}/M_{\star})^{1/3}v_{\star} \gg v_{\star}$, where $v_{\star} = \sqrt{GM_{\star}/R_{\star}}$ is the breakup rotational velocity of the star. For example, a Solar-type star near the MBH of the Milky Way can reach $v(r_t) = \sqrt{2r_g/r_t} \gtrsim 0.3c$ (Section 1.4). These extreme velocities have several implications. Stellar encounters at $v \gg v_{\star}$ are too fast for efficient exchange of energy or angular momentum at impact parameters larger than R_{\star} (cf. Equation 1), and therefore two-body relaxation is suppressed inside the collision radius, r_{coll} , where the velocity dispersion $\sigma^2 \sim GM_{\bullet}/r$ satisfies $\sigma(r_{\text{coll}}) \sim v_{\star}$ (Section 2.1). Direct stellar collisions are destructive, because the kinetic orbital energy at infinity of the colliding stars exceeds the stellar binding energy (Section 6.1). Likewise, binaries cannot survive three-body ionization because even a contact binary is not bound enough compared with the typical velocity of a field star (Section 6.2). The high velocity affects also three-body interactions of a binary with the MBH, because if the binary is tidally separated, one of the two stars is ejected as a hypervelocity star (HVS) with velocity $\sim \sqrt{vv_{\star}}$ (Hills 1988, Yu & Tremaine 2003), which can exceed the escape velocity from the host galaxy (Section 4.4.1).

1.4. The Special Role of the Galactic MBH Sgr A*

Sgr A*, the $M_{\bullet} \simeq 4 \times 10^6 M_{\odot}$ MBH at the center of the Milky Way, $R_0 \simeq 8 \text{ kpc}$ from the Solar System (Gillessen et al. 2009, Boehle et al. 2016), is the nearest MBH to us. Closer by a factor

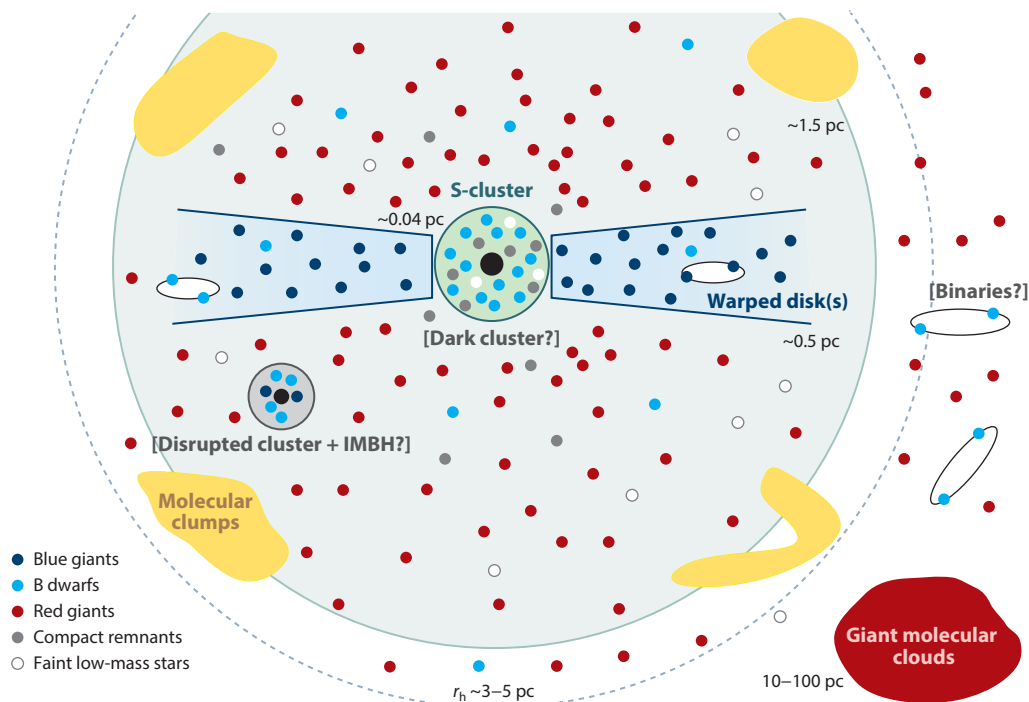


Figure 1

A not-to-scale diagram of the environment of the Galactic MBH in the center of the Milky Way (Alexander 2011). Stars are denoted by the small circles, color-coded by spectral type; binaries are denoted by two stars on an ellipse; and gas clouds are denoted by irregular-shaped blobs. Objects labeled by [...] indicate that their existence is unconfirmed or controversial. The MBH at the center (*large black circle*) extends its direct dynamical influence up to $r_h \sim 3\text{--}5$ pc. There is very little gas inside r_h , apart from a ring-like structure of massive molecular clumps at $r \sim 1.5$ pc. Further out beyond r_h on the 10–100-pc scale there are $\mathcal{O}(10^8)$ stars, multiple GMCs, and presumably also young binaries (Perets et al. 2007), which can be efficiently scattered by the GMCs toward the MBH, and undergo tidal capture and hypervelocity ejection (Section 4.4). Inside r_h , the stellar population is a mix of old red giants, in an approximately isotropic distribution, and of young stars, mostly in two distinct populations: $\mathcal{O}(100)$ massive OB stars in a warped, coherently rotating stellar disk, extending between ~ 0.04 pc (1 arcsec) and ~ 0.5 pc, and ~ 30 MS B stars on isotropic orbits inside ~ 0.04 pc (the so-called S-star cluster). Still unclear is the distribution of the long-lived, low-mass faint MS stars, which are currently below the detection threshold, and of the dark stellar remnants, in particular the $\mathcal{O}(10 M_\odot)$ stellar BHs (the hypothetical dark cusp). The presence of an IMBH companion to Sgr A*, if light and distant enough, cannot yet be excluded (Gillessen et al. 2009). Abbreviations: BH, black hole; GMC, giant molecular cloud; IMBH, intermediate-mass black hole; MBH, massive black hole; MS, main sequence.

of ~ 100 than the MBH in Andromeda, and by a factor of $\sim 2,000$ than MBHs in the nearest galaxy cluster Virgo, Sgr A* is by far the most accessible to high-resolution observations, in spite of the very strong dust extinction on the line of sight through the Galactic disk (Schödel et al. 2007). Major instrumental and observational advances in the IR and X-ray bands over the past few decades have made it possible to observe faint accretion emission from the MBH and accurately track individual stars and gas clumps by imaging and spectroscopy as they orbit around it (see the review by Genzel et al. 2010). The wealth of detail, the precision, and the depth of observations of Sgr A* (**Figure 1**) are unlikely to be matched for other MBHs any time soon. The Copernican principle suggests that galactic nuclei in general are as complex as the Galactic Center. Therefore, the MBH at the center of the Milky Way plays crucial roles as a source of information on the environment of MBHs, as a driver of efforts to understand galactic nuclei, and as a test bed for developing theories and models.

SN: supernova

EMRI: extreme
mass-ratio inspiral
event

The central 1 pc of the Galactic Center contains a mixture of low-mass red old stars (only the red giants are currently detectable) and massive blue stars, the products of recent star formation (Bartko et al. 2010). Many of the blue stars orbit in a coherent disk-like configuration (Levin & Beloborodov 2003) and appear to have been formed ~ 6 Myr ago from a fragmenting, self-gravitating circumnuclear gas disk, with an unusually flat top-heavy initial mass function, quite unlike that observed in star-forming regions in the galactic bulk (Nayakshin & Sunyaev 2005, Bartko et al. 2010, Lu et al. 2013). The observed blue OB giants will eventually explode as supernovae (SNe) and populate the Galactic Center with compact remnants (SN remnants are still seen in the region; e.g., Maeda et al. 2002). There is further evidence that episodic top-heavy star formation has been going on in the inner nucleus over the past 12 Gyr at a roughly constant rate (Maness et al. 2007). This implies that the local stellar population that interacts with the MBH may be quite different than that of the field.

The Galactic MBH is near the lower limit of MBH masses detected to date (Kormendy & Ho 2013), in keeping with the M_*/σ relation and the relatively low-mass bulge of the Milky Way. The paucity of Sgr A*-like MBHs may reflect the strong selection bias against low-mass MBHs. By its relatively low mass, Sgr A* is expected to be surrounded by a dense cusp of dynamically relaxed old stars (Section 2.1). However, this is not observed in the distribution of the red giants ($K \lesssim 16^m$) (Buchholz et al. 2009, Do et al. 2009, Bartko et al. 2010), which are currently the only directly detectable tracers of the faint old population. Instead of rising, the red giant distribution is observed to flatten or even dip toward the center. Whether this implies that the faint old population and its associated compact remnants is indeed missing, for example, ejected by a fairly recent major merger (Merritt 2010), or whether this is merely the result of a selective destruction of red giant envelopes (e.g., Amaro-Seoane & Chen 2014) is still unclear. However, the low mass of Sgr A*, the absence of other evidence for a past major merger, and the fast relaxation expected by the presence of stellar BHs in the system (Section 2.1, Preto & Amaro-Seoane 2010) argue against the likelihood of a major merger in the recent past of the Milky Way, or the possibility that an earlier one left the system out of dynamical equilibrium up to the present day (Alexander 2011). It should be noted that a high-density dark cusp of stellar remnants (primarily stellar BHs) can develop on timescales that are much shorter than the overall relaxation time (Preto & Amaro-Seoane 2010, Antonini 2014).

The question of the stellar density and the dynamical state around Sgr A* is important because the rate of strong interactions with the MBH scales with the stellar density close to it. In particular, the Milky Way serves, by a coincidence of technology,³ as the archetypal nucleus for cosmic sources of low-frequency GWs from stellar BHs inspiraling into an MBH (extreme mass-ratio inspiral events, EMRIs), which are targets for planned spaceborne GW detectors. [The central role of the Milky Way in the planning of such experiments is reflected by the fact that the target galactic nuclei are sometimes denoted Milky Way equivalent galaxies (MWEGs).] The numbers and dynamics of stars and compact objects in the inner few $\times 0.01$ pc of Sgr A* therefore have, by extrapolation, direct bearings on the predicted cosmic low-frequency GW event rates (Section 5.1).

A recent reanalysis of deep number counts ($K \sim 18^m$, dominated by old subgiants; Schödel et al. 2007, their figure 16) and of the diffuse light distribution shows a cusp that rises from ~ 3 pc to the inner few $\times 0.01$ pc, with $\rho_* \sim 10^7 (r/0.1 \text{ pc})^{-1.20} M_\odot \text{ pc}^{-3}$ (Schödel et al. 2016). If confirmed, this would imply that the missing cusp problem is actually a problem of the missing brighter red giants in the inner < 0.1 pc and that these do not trace the old faint population.

³The longest laser interferometric baseline that can be reliably maintained in space at present is $\mathcal{O}(10^6 \text{ km})$, which has maximal sensitivity to GWs in the 1–10 mHz range. This corresponds to GWs emitted from near the horizon of an $\mathcal{O}(10^6 M_\odot)$ MBH (Amaro-Seoane et al. 2007).

Finally, the Galactic Center offers a unique opportunity to detect phenomena whose observational signature is presently too subtle to be observed in more distant nuclei. These include very close star–star encounters that lead to a stochastic spin-up and mixing of long-lived stars near MBHs (Alexander & Kumar 2001); near-miss tidal interactions between stars and the MBH, which result either in strong tidal scattering that perturbs the internal structure and affects the evolution of a substantial fraction of stars inside r_h (Alexander & Livio 2001, Manukian et al. 2013) or in orbital decay as ultraluminous tidally powered “squeezars” (Alexander & Morris 2003) or in tidal stripping of tenuous envelopes of extended stars (a possible interpretation of the tidally sheared G2 cloud; Gillessen et al. 2012, Phifer et al. 2013, Guillochon et al. 2014). A prime objective of observations of Sgr A* and its environment is to detect subtle post-Newtonian effects and test strong gravity (Section 5.2).

1.5. Scope of This Review

This review focuses on galactic nuclei that harbor a single MBH in the lower-mass range ($M_\bullet < 10^8 M_\odot$) and on the role stellar dynamics play in enabling and regulating the unusual stellar phenomena that occur near the MBH.

There are theoretical and practical reasons to focus specifically on this subclass of galactic nuclei, beyond the fact that lower-mass galactic nuclei, which are associated with lower-mass MBHs, are the most numerous (Li et al. 2011). Such systems, if they evolve in isolation, can reach dynamical quasi-equilibrium by stellar two-body relaxation (Preto & Amaro-Seoane 2010, Bar-Or et al. 2013). In that case, the steady-state configuration is independent of the unknown initial conditions, and so it is possible, ideally, to deduce it from first principles and apply results generally to all relaxed nuclei. Because the quasi-steady state is long-lived, relaxed galactic nuclei are statistically the most likely to be observed (assuming the relaxation time is substantially shorter than the age of the Universe). Note, however, that there is no guarantee that dynamically relaxed galactic nuclei form a considerable fraction of the population; the assumption of isolated evolution is a matter of boundary conditions that, like initial conditions, are generally hard to determine reliably or justify robustly in astrophysical contexts. Another unrelated physical property that characterizes MBHs with mass below $10^8 M_\odot$ and makes them more interesting is that they tidally disrupt MS stars outside of the event horizon (Section 1.3.2), which allows the eruption of an observable tidal flare.

There are also practical reasons to focus on nuclei with $M_\bullet < 10^8 M_\odot$. The overlap of this mass range with the Galactic MBH Sgr A* means that extrapolations of its properties are more likely to be justified, and the technological coincidence of this mass range with the sensitivity of planned spaceborne interferometric GW detectors (Section 1.4) makes it of particular relevance for GW physics.

Other recent reviews that complement and expand the material covered here are by Alexander (2005, a theoretical review on the stellar processes in the Galactic Center), Genzel et al. (2010, an observational review on the Galactic Center), Graham (2016, the MBH–host galaxy connection), Miller & Colbert (2004, IMBHs), Amaro-Seoane et al. (2007, detection of GWs from EMRIs by space interferometers), Merritt & Milosavljević (2005, binary MBHs), and Volonteri (2010, formation of MBHs). Comprehensive textbook-level coverage of stellar dynamics on galactic and nuclear scales can be found in Binney & Tremaine (2008) and Merritt (2013).

2. DYNAMICAL RELAXATION NEAR AN MBH

Close enough to the MBH, inside the radius of influence, r_h , where the total stellar mass is small, $N_\star M_\star / M_\bullet \ll 1$, but far enough that the system is Newtonian, $r/r_g \gg 1$, the mass of the MBH

Table 1 Hierarchy of relaxation processes

Process	NR	Scalar RR	Vector RR
Effective particles	Points	Ellipses	Annuli
Averaged quantity	None	Mean anomaly	Arg. of periapse
Conserved quantity	None	E	E, J
Coherence time	$T_c^{\text{NR}} < P$	$P < T_c^{\text{RR}} \sim T_c^{\text{M}} < T_p^{(a)}$	$T_p^{(a)} < T_c^{\text{RR}} \sim T_c^{\text{SQ}}$
Residual rms force	$\sqrt{N_\star} GM_\star \sqrt{Q/a^2}^{(b)}$	$\sqrt{N_\star} GM_\star / a^2$	$\sqrt{N_\star} GM_\star / a^2$
Relaxation time ^(c)	$Q^2 P / N_\star \log Q^{(b)}$	QP	$QP / \sqrt{N_\star}$

^a T_p is the test star's precession period.

^bIntegrated over all impact parameters.

^c $T_{\text{relax}} \sim J_c^2 / \langle \tau_N^2 \rangle T_c$.

Abbreviations: NR, nonresonant (two-body) relaxation; rms, root-mean-square; RR, resonant relaxation.

dominates the potential and the dynamics are approximately Keplerian over timescales much longer than the Keplerian orbital timescale $P = 2\pi\sqrt{a^3/GM_\star}$.⁴ The discussion here focuses on how such a system “forgets” its initial conditions and approaches quasi-steady state. The true steady state of a self-gravitating system is that of maximal inhomogeneity: a small dense central system (a binary) and an unbound halo at infinity (e.g., Binney & Tremaine 2008). The evolutionary time to achieve this steady state is usually much longer than the Hubble time t_H . It is more meaningful to consider the quasi-steady state of the system over t_H , which for brevity is denoted here as steady state.

The primary parameters that determine the steady state are the ratio of MBH mass to the mean stellar mass, $Q = M_\bullet / \langle M_\star \rangle$, and N_h , the total number of stars enclosed within r_h . The secondary parameters are the root-mean-square (rms) of the stellar mass function, $\langle M_\star^2 \rangle^{1/2}$ and the stellar density distribution inside r_h , which is approximated here as a power law with logarithmic slope α , so that $N_\star(< r) = N_h(r/r_h)^{3-\alpha}$ and $n_\star(r) \propto r^{-\alpha}$.

Two-body relaxation is inherent to motion in a potential generated by discrete objects. In the impulsive limit, the force a perturbing star exerts on a test star at nearest approach, over a small fraction of the test star's orbit, deviates substantially from the superposed force of the entire system, which governs motion on timescales shorter than the relaxation time. Over time, the cumulative effect of such uncorrelated two-body gravitational interactions randomizes both the orbital energy and angular momentum. This slow but unavoidable noncoherent collisional relaxation process⁵ can be described as diffusion in phase space in terms of the Fokker–Planck (FP) equation (Section 2.1). In the opposite limit of very soft encounters, where the nearest approach of the perturbing star is larger than the orbit of the test star, it is no longer valid to describe the interaction as occurring instantaneously and locally between two stars. Rather, the long-term temporal correlations of the perturbing background in the near-symmetric potential near an MBH drive a different form of randomization: resonant relaxation (RR, or coherent relaxation; Section 2.2). These two limits of relaxation can be incorporated in a unified framework (Section 2.3; **Table 1**).

⁴The typical radius r , the Keplerian semimajor axis a , and the circular radius corresponding to orbital energy E are used here interchangeably in approximate derivations and relations.

⁵Partial randomization occurs also in collisionless systems by phase mixing (including violent relaxation and Landau damping) and chaotic mixing. However, the general properties of the end states of these processes are not yet well understood. (Mo et al. 2010).

FP: Fokker–Planck

RR: resonant
relaxation

2.1. Noncoherent Relaxation

Unavoidable noncoherent two-body encounters guarantee a minimal relaxation rate in a stellar system. The simple case in which all the stars have the same mass is discussed first, and then the implications of a stellar mass spectrum are considered.

sma: semimajor axis
NR: nonresonant
(two-body) relaxation

2.1.1. Two-body relaxation. A test star orbiting with semimajor axis (sma) a around a central mass M_* surrounded by stars of mass M_* and space density n_* is subject to a net residual specific force $\sqrt{\langle F^2 \rangle} \sim \sqrt{dN_*} GM_*/b^2$ from the $dN_* \sim n_* b^2 db$ stars in a thin shell of radius $b \ll a$ around it, due to the Poisson fluctuations about the mean density. The residual force persists until the stars generating it move substantially, after a short coherence time $T_c^{\text{NR}} \sim b/\sigma \ll a/\sigma \sim P(a)$, where $\sigma^2 \sim GM_*/a$ is the velocity dispersion. Because $T_c^{\text{NR}} \ll P$, the encounter is impulsive (a collision). The short duration of the interaction and the fact that successive collisions involve different perturbers justify the assumption that the perturbations are a Markovian (memoryless) process, and this allows their cumulative effect to be described as diffusion. The diffusion timescale for both energy and angular momentum is $T_E = E^2/D_{EE} \sim J_c^2/D_{JJ}$, where $J_c = \sqrt{GM_* a}$ is the circular angular momentum, and D_{EE} and D_{JJ} are the energy and angular momentum diffusion coefficients.

It is also useful to define relaxation in terms of quantities in position and velocity space. The impulse to the test star by a single collision is $\delta v \sim \sqrt{\langle F^2 \rangle} T_c^{\text{NR}}$. These accumulate noncoherently over times $t > T_c^{\text{NR}}$ to $\langle \Delta v^2 \rangle \sim (G^2 M_*^2 n_*/\sigma) db/b$. Integration over all shells from b_{\min} to b_{\max} assuming constant n_* yields the noncoherent (two-body) relaxation time, also known as the Chandrasekhar time,

$$T_{\text{NR}}(r) = \frac{\sigma^2}{\langle \Delta v^2 \rangle} \sim \frac{\sigma^3}{G^2 M_*^2 n_* \log \Lambda} \sim \frac{Q^2 P(r)}{N_*(r) \log Q}, \quad (1)$$

where $\Lambda = b_{\max}/b_{\min}$ is the Coulomb factor, and the last approximate equality holds when the system is dominated by a central MBH, in which case $\Lambda \sim Q$ (Bar-Or et al. 2013). The Coulomb logarithm lies in the range $14 \lesssim \log Q \lesssim 23$ over the known range of MBH masses. $T_{\text{NR}} \propto r^{\alpha-3/2}$ is typically a weak function of radius when a stellar cusp surrounds the MBH (Section 2.1.4).

The time for the stellar system around an MBH to recover from a perturbation and return to steady state can be expressed in terms of quantities at the radius of influence as (Bar-Or et al. 2013)

$$T_{\text{ss}} \simeq 10 T_E(r_h) \simeq \frac{5}{32} \frac{Q^2 P_h}{N_h \log Q}. \quad (2)$$

Although the diffusion timescale $T_E(E, J)$, the Chandrasekhar [nonresonant (two-body) relaxation, NR] time $T_{\text{NR}}(r)$, and the relaxation time T_{ss} (at r_h) all express the tendency of the system to evolve toward steady state, their numerical values near an MBH are quite different, $T_{\text{NR}}(r_h) \sim 4 T_{\text{ss}} \sim 40 T_E$ (Bar-Or et al. 2013). This distinction matters because often T_{ss} is not clearly different from the age of the system, and inferences about the dynamical state then depend sensitively on the precise definitions and values of these timescales.

2.1.2. Anomalous diffusion. Past attempts to measure the NR rate and the approach to steady state in numeric experiments resulted in diverging estimates of the dynamical state inside the radius of influence, especially close to the MBH (cf. the discrepancy between Bahcall & Wolf 1977 and Madigan et al. 2011). The likely cause is that relaxation by gravitational interactions is not a true diffusion process but rather a marginal case of anomalous diffusion (Bar-Or et al. 2013),

GMC: giant
molecular cloud
DF: distribution
function

which is very slow to converge and therefore difficult and misleading to measure by standard methods.

The statistical evolution of the stellar orbital energy distribution is expressed by the energy propagator function, which describes the evolution of an initially monoenergetic distribution of stellar energies. For true diffusion, the propagator converges quickly by the central limit theorem to a Gaussian, whose width grows as $\sqrt{D_{EE}t}$. In that limit the process is fully described by the two lowest-order diffusion coefficients (drift and scatter). However, the Markovian assumption of independent scattering events is not sufficient to ensure the applicability of the central limit. In addition, the mean and variance of the propagator must be finite. This loophole (diverging moments) allows certain physical processes to display a slowly converging anomalous diffusion. In those cases the probability distribution of the propagator is heavy-tailed; impossibly large changes (when estimated naively by Gaussian distribution standards) actually do occur surprisingly frequently, and all higher-order diffusion coefficients contribute to the evolution. Gravitational scattering happens to be one such anomalous process with a formally diverging variance due to the $r \rightarrow 0$ divergence of the gravitational potential of a point mass (Goodman 1983). This makes energy relaxation by gravitational interactions a marginally anomalous diffusion process, with a heavy-tailed distribution that initially grows as $\sim \sqrt{t \log(t)}$ (Bar-Or et al. 2013). Because no physical process can truly diverge, the propagator must eventually converge to a Gaussian. Careful analysis shows that this occurs well before the MBH/nucleus system reaches steady state (Equation 2). However, it can affect the nature of gravitational perturbations on short timescales. For example, it may be detected by future high angular resolution observations of stellar orbits near Sgr A* (Bar-Or et al. 2013). The relevance of anomalous diffusion for angular momentum evolution remains to be studied.

2.1.3. Massive perturbers. The derivation of the two-body relaxation timescale (Equation 1) is easily generalized to the realistic case in which the stellar population has a spectrum of masses, $M_*^2 n_* \rightarrow \langle M_*^2 \rangle n_*$. Because $\langle M_*^2 \rangle \geq \langle M_* \rangle^2$, a mass spectrum always implies faster relaxation than estimated by naively substituting $M_* \rightarrow \langle M_* \rangle$. In particular, relaxation can be extremely fast if the system contains a few massive perturbers [for example, giant molecular clouds (GMCs), clusters, or IMBHs], with mass $M_p \gg M_*$ (Spitzer & Schwarzschild 1951). In that case, the quadratic dependence on the mass typically more than compensates for the low space density of the massive perturbers, n_p , and NR is accelerated by $T_{NR,*}/T_{NR,p} \sim M_p^2 n_p / \langle M_*^2 \rangle n_* \gg 1$. For example, GMCs in the Galactic Center accelerate relaxation by a factor of 10^4 – 10^6 compared with relaxation by stars (Perets et al. 2007). However, the effectiveness of a gravitational encounter with extended massive perturbers (GMCs or clusters) is suppressed logarithmically by a factor $\log \Lambda_{\text{extended}} / \log \Lambda_{\text{point}}$ because close (penetrating) encounters involve only a fraction of the extended perturber’s mass. For the relaxation of a point-like object (a star, or a binary when treated as if concentrated at its center of mass), this suppression is a small correction only. However, for the relaxation-like process of binary evaporation (Section 6.2), extended massive perturbers are inefficient when their size far exceeds the binary sma. Note that the presence of massive perturbers is relevant only when stellar NR alone is too slow to bring the system to full randomization. An example of this distinction is the modest increase due to massive perturbers in the stellar TDE rate (Section 4.2), as opposed to the huge boost in the binary tidal separation rate (Perets et al. 2007) (Section 4.4.1).

2.1.4. Steady-state stellar cusp. The steady-state density distribution of a spherical Keplerian system of single-mass stars around an MBH is approximately a power-law cusp, $n_* \propto r^{-7/4}$ [the distribution function (DF) is $f(E) \propto E^{1/4}$] (Bahcall & Wolf 1977). The Bahcall–Wolf solution

averages over angular momentum and describes the stellar current to the MBH, I_* , in energy only.⁶ Stars fall in the MBH when they cross below some threshold a_* . This approximation captures quite well the solution in the intermediate range $R_* \ll r \ll r_h$, as verified by more detailed calculations (e.g., Bar-Or & Alexander 2016). The Bahcall–Wolf solution is similar to the $I_* = 0$ (zero current) solution that holds in the limit of a closed system, in which the stellar current at a_h is set to zero, and the limit $a_*/a_h \rightarrow 0$ (no sink) is assumed. That this solution also describes a realistic open system appears at odds with the very large natural scale for the stellar diffusion current in the system, $I_* \sim \mathcal{O}(N_*/T_E)$. However, this is when $a_*/a_h \ll 1$, the drift and scatter currents are near zero,⁷ and therefore $0 < I_* \ll I_*$.

2.1.4.1. Dynamical friction. Two-body NR scattering (described by the second-order diffusion coefficient, the scatter, which depends only on the mass spectrum of the background stars because all test masses accelerate similarly) is balanced by dynamical friction (described by the first-order diffusion coefficient, the drift, which is proportional to the test mass because it determines how massive the wake is that forms behind the test star and drags it). The deceleration, due to the drift of a massive test mass $M \gg \langle M_* \rangle$ moving slowly relative to the background, scales with v (e.g., Binney & Tremaine 2008), and so dynamical friction acts like viscous dissipation. As the test mass slows down, it sinks further in the potential until it either “runs out” of stars (the stellar mass enclosed in its orbit is smaller than M) (e.g., Merritt 2013) or reaches the tidal disruption radius or event horizon and is destroyed.

2.1.4.2. Mass segregation. Realistic stellar populations have a broad mass spectrum. Dynamical friction in the steep MBH potential frustrates the trend toward equipartition, because when the massive stars slow down, they sink inward. Conversely, light masses speed up and migrate to wider orbits. Mass segregation modifies the single-mass power-law Bahcall–Wolf solution. Every mass bin $M_* dM_*$ is characterized by its own power-law density profile $n_{M_*} \propto r^{-\alpha_{M_*}}$, where the larger α_{M_*} is, the more massive is the star, with $3/2 \lesssim \alpha_{M_*} \lesssim 5/2$ (Bahcall & Wolf 1977, Alexander & Hopman 2009, Keshet et al. 2009). The quasi-steady state of a mass-segregated cusp can still be approximated by a Maxwell–Boltzmann mass-dependent velocity distribution (Alexander & Kumar 2001), but the spread in velocities is much reduced compared with equipartition, $\sigma_{M_*}^2(r) = GM_*/(1 + \alpha_{M_*})r$ (Alexander 1999).

2.1.4.3. Weak versus strong mass segregation. The mass segregation steady-state solution has two branches, depending on the stellar mass function. In the Bahcall & Wolf (1977) weak segregation solution the approximate power-law density distribution has a mass-dependent logarithmic slope, $\alpha(M_*) = 3/2 + (M_*/\max M_*)/4$. Thus the heaviest stars assume the $\alpha_H = 7/4$ power law of a single-mass population, whereas the lightest stars have a somewhat less centrally concentrated distribution with $\alpha_L = 3/2$ ($\alpha_H - \alpha_L = 1/4$). The full range of steady-state mass segregation solutions depends on the mass function of the stellar population (Alexander & Hopman 2009). Long-lived stellar populations, whether old star-burst or continually star-forming ones, are well approximated by a two-mass population: the $M_L \sim \mathcal{O}(1 M_\odot)$ light stars with a number density N_L

⁶The steady-state Bahcall–Wolf solution can be derived qualitatively by assuming that the orbital energy lost by stars that are scattered into the MBH is carried outward by the stellar system on the NR timescale (e.g., Binney & Tremaine 2008).

⁷Such a steady-state solution, or one where $I_* = 0$ is realized by a cancellation between large drift and scatter currents, requires a delicate balance between the drift and scatter coefficients. Slight deviations from the true form of the diffusion coefficients (e.g., when they are not known exactly and must be derived empirically from N -body simulations or from approximate physical arguments) can lead to large errors in the steady-state DF and/or unrealistically large currents $I_* \sim \mathcal{O}(I_*)$.

NS: neutron star

in the unsegregated unbound population, which includes low-mass MS stars, WDs and neutron stars (NSs), and the $M_{\text{H}} \sim \mathcal{O}(10 M_{\odot})$ heavy remnants, with number density N_{H} , which consists of stellar BHs. The nature of the mass segregation solution depends on the value of the the relaxational parameter $\Delta = 4N_{\text{H}}M_{\text{H}}^2/[N_{\text{L}}M_{\text{L}}^2(3 + M_{\text{H}}/M_{\text{L}})]$, which measures the relative strength of heavy-on-heavy scattering to heavy-on-light dynamical friction (Alexander & Hopman 2009). The weak segregation solution applies when $\Delta \gg 1$. In that case the heavy stars are the dominant component of the population, interactions with the light stars are negligible, and the heavy stars behave as a single-mass population. The strong segregation solution applies when $\Delta \ll 1$. In that case the heavy stars are a trace component of the population, and therefore they interact mainly with the light stars, and are driven efficiently to the center by dynamical friction. [This is different, and in the opposite sense from the Spitzer (1969) instability in a cluster without an MBH, where a dominant stellar BH population segregates and forms a dense central subsystem.] The strong segregation solution leads to steeper slopes and a larger difference between the light and heavy masses, $2 \lesssim \alpha_{\text{H}} \lesssim 11/4$ and $3/2 < \alpha_{\text{L}} < 7/4$ ($\alpha_{\text{H}} - \alpha_{\text{L}} \simeq 1$). The general mass segregation solution for an arbitrary mass function can have an even steeper density profile slope, $\alpha(\max M_{\star}) = 5/2$ (Keshet et al. 2009). These analytic results were confirmed by N -body simulations (Preto & Amaro-Seoane 2010). Long-lived stellar populations have $\Delta < 0.1$, and therefore many relaxed galactic nuclei are expected to be strongly segregated, and have steep high-density cusps of stellar BHs. This is true in particular for the Galactic Center (Morris 1993). **Figure 2** shows the strong mass segregation that is predicted for the stellar BHs in a Milky Way-like galactic nucleus. Strong mass segregation of stellar BHs increases the EMRI rate by a factor of ten by concentrating more BHs below the critical s_{ma} for inspiral (Section 3.1.2).

2.1.4.4. The drain limit. A useful upper limit on the number of stars that can exist in quasi-steady state inside a small volume around an MBH can be obtained by requiring that the mean time for two-body interactions to scatter a star into the MBH be longer than the age of the system. The drain limit (Alexander & Livio 2004) is given by the condition $N_{\star}^{-1} dN_{\star}/dt = [\log(\sqrt{2r/r_{\text{g}}})T_{\text{NR}}(r)]^{-1} = t_{\text{H}}^{-1}$ (Section 3.1). The solution, $\max N_{\star}(r)$, is the maximal number of stars that can be initially

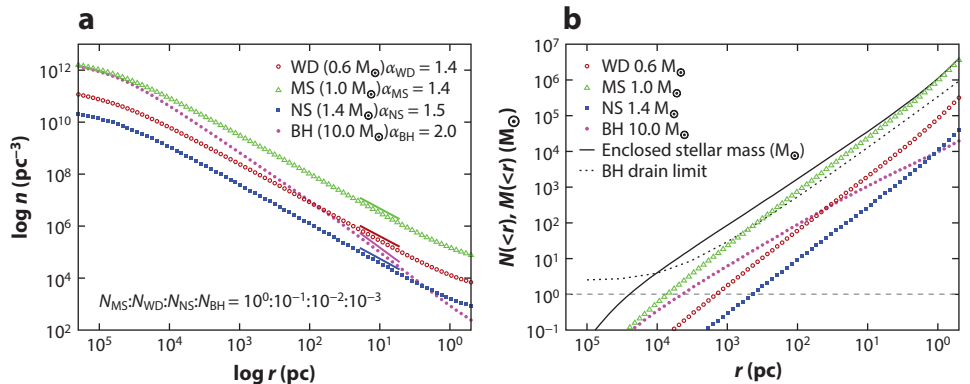


Figure 2

The effects of strong mass segregation on the density distribution of a simplified population with MS stars and remnants (WDs, NSs, and stellar BHs) around a Milky Way-like nucleus with $M_{\bullet} = 4 \times 10^6 M_{\odot}$ (Alexander & Hopman 2009). (a) The number density and approximate power-law indices (evaluated over the intermediate range indicated by the short solid lines) for the distributions of stars and remnants. (b) The enclosed mass as a function of radius, and the drain limit upper bound for stellar BHs (Equation 3). Abbreviations: BH, black hole; MS, main sequence; NS, neutron star; WD, white dwarf.

packed inside r with a survival probability of $1/2$ over t_H (assumed to be the age of the system),

$$\max N_*(< r) \sim \frac{2}{3} \frac{\log \sqrt{2r/r_g}}{\log Q} \frac{M_\bullet^2}{\langle M_\bullet^2 \rangle} \frac{P(r)}{t_H}. \quad (3)$$

The dependence on $\langle M_\bullet^2 \rangle^{-2}$ reflects the acceleration of the relaxation process in the presence of a mass spectrum (Section 2.1.3). Comparison with detailed calculations (e.g., Deegan & Nayakshin 2007) shows that the drain limit is a somewhat conservative upper bound (by up to a factor of a few at $r \ll r_h$; cf. Figure 2).

2.1.5. Dynamically relaxed galactic nuclei. The empirical M_\bullet/σ relation (Section 1.2), $M_\bullet \propto \sigma^\beta$, implies a scaling for the two-body relaxation time of galactic nuclei. Because the MBH's radius of influence scales as $r_h \sim GM_\bullet/\sigma^2 \propto M_\bullet^{1-2/\beta}$ and the number of stars inside r_h scales as $N_h \propto Q$, the time to reach steady state (Equation 2) at the radius of influence scales as $T_{ss} \propto Q^2 P_h / N_h \propto M_\bullet^{2-(3/\beta)}$ (omitting the logarithmic Coulomb factor) (Alexander 2011). The relaxation time thus increases with the MBH mass for $\beta > 1.5$. The M_\bullet/σ relation also implies that the mean stellar density inside r_h scales as $\bar{n}_* \sim 3Q/4\pi r_h^3 \propto M_\bullet^{(6/\beta)-2}$, which falls with the MBH mass for $\beta > 3$. The empirically determined range $\beta \sim 4-5$ then means that isolated galactic nuclei with lower-mass MBHs have denser, more relaxed nuclei. A detailed study of the relaxation process, which fixes the exact numeric prefactors that enter T_{ss} (Bar-Or et al. 2013), shows that galactic nuclei with $M_\bullet < \text{few} \times 10^7$, which evolve passively in isolation, should be dynamically relaxed by t_H . This conclusion is further reinforced when the accelerating effect of massive stars is taken into account (Preto & Amaro-Seoane 2010).

2.2. Resonant Relaxation (Coherent Relaxation)

RR is a rapid angular momentum relaxation mechanism that operates in symmetric potentials, which restrict orbital evolution (Rauch & Tremaine 1996, Hopman & Alexander 2006). In particular, an MBH enforces a high degree of symmetry on the gravitational potential at $r \ll r_h$. In the Keplerian limit, where both star–star interactions and GR are negligible, stars move on fixed ellipses around the MBH. Assume that the orbital parameters of a test star are statistically similar to those of the background (this is later relaxed in Section 3.2). Even when the stellar distribution is spherical and isotropic on average, Poisson fluctuations due to the finite number of stars generate a nonzero residual force field that acts on the test star, with rms $F_N \sim \sqrt{N_*(a)} GM_*/a^2$. The restricted orbital evolution on timescales much longer than the radial orbital period P allows the phase averaging of the residual force over P (the mean anomaly) of both the test star and the background. This implies that the phase-averaged force conserves the orbital energy of the test star.⁸ In the case of a nearly Keplerian system, the phase-averaged orbits can be conceptualized as fixed mass wires, whose total mass is that of the star, and whose linear mass density is inversely proportional to the local orbital velocity.

The residual rms torque on the test star, $\tau_N \sim a F_N \sim \sqrt{N_*(a)} GM_*/a$, persists as long as the background orbits remain fixed, over a coherence time T_c . The coherence time is limited by the fastest process that breaks the symmetry and randomizes the background. The relevant processes for a symmetric stellar cusp around a nonspinning MBH are the (a) retrograde precession of the argument of periastron due to the enclosed stellar mass inside the orbit (mass precession), which

⁸This is formally expressed by double averaging the Hamiltonian that describes the MBH–star and the star–star interactions in terms of action-angle canonical coordinates over the mean anomalies of the test star and background stars. The conjugate action of the test star $I = \sqrt{GM_* a}$ is then conserved, and therefore so is its orbital energy (Bar-Or & Alexander 2014).

SRR: scalar resonant relaxation

VRR: vector resonant relaxation

drops to zero for $j \rightarrow 0$ (radial) orbits and grows larger as $a \rightarrow r_h$, (b) in-plane prograde GR precession of the argument of periastron (Schwarzschild precession), which is larger the smaller the orbital periastron, that is, larger for $j \rightarrow 0$ and $a \rightarrow 0$ orbits, and (c) ultimately, the residual torques themselves randomize the background orbits (self-quenching), because any star in the system can play the role of a test star. The mass precession coherence time is $T_c^M(a) \sim QP(a)/N_*(a)$, the isotropically averaged GR precession time is $T_c^{\text{GR,iso}}(a) = (a/12r_g)P(a)$, and the self-quenching coherence time is $T_c^{\text{SQ}}(a) \sim QP(a)/\sqrt{N_*(a)}$ (e.g., Hopman & Alexander 2006). The effective extent of an $n_* \propto r^{-\alpha}$ background that exerts a coherent torque on a star with sma a is $\lesssim 2^{2/(3-\alpha)}a$ (Bregman & Alexander 2009), as demonstrated numerically by Gürkan & Hopman (2007). For typical values of α , the spatial coherence of the RR torques is $\Delta \log a \sim 1$. The exact numeric prefactors relating the system parameters to the resonant torques and coherence times are difficult to derive analytically, but they can be calibrated by simulations (Rauch & Tremaine 1996, Eilon et al. 2009, Kocsis & Tremaine 2015, Bar-Or & Alexander 2016).

On times shorter than T_c , the change in the angular momentum of the test star grows linearly with time up to $(\Delta J)_c = \tau_N T_c$. This maximal coherent change then becomes the mean free path for a random walk in angular momentum phase space on times longer than T_c , $|\Delta J(t)| = |(\Delta J)_c| \sqrt{t/T_c}$. It is convenient to normalize the evolution in angular momentum to $J_c(a)$ and define the relaxation timescale as the time for the relative change to reach order unity, $T_{\text{RR}} = J_c^2/(\tau_N^2 T_c)$, so that $\Delta j(t) = \sqrt{t/T_{\text{RR}}}$. In terms of the system parameters (cf. Equation 1),

$$T_{\text{RR}}(a) = \frac{J_c^2(a)}{\tau_N^2(a) T_c(a)} \sim \frac{Q^2}{N_*(a)} \frac{P^2(a)}{T_c(a)} \sim \left[\frac{P(a)}{T_c(a)} \log Q \right] T_{\text{NR}}(a). \quad (4)$$

Unlike NR, where two-body relaxation is boosted by diverging local point–point interactions, as expressed by the Coulomb factor, RR proceeds by the interaction of extended objects (the mass wires), whose mutual torques do not diverge but are rather boosted by the long coherence time. RR is significant for dynamics near an MBH because the coherence time there can be many orders of magnitude longer than the orbital time, whereas $\log Q \sim \mathcal{O}(10)$, and therefore $T_{\text{RR}} \ll T_{\text{NR}}$ (Equation 4). Because $j \rightarrow 0$ orbits lead to strong interactions with the MBH, rapid angular momentum relaxation by RR can potentially dominate the dynamics leading to such interactions.

The residual torque due to the superposed forces of many wires changes both the direction and magnitude of the test star’s angular momentum. Such an RR process is denoted (confusingly) scalar RR (SRR), to emphasize that it changes j , and in particular can drive it to $j \rightarrow 0$. The coherence time of SRR is set by the combined in-plane retrograde mass precession and prograde GR precession, $T_c^{\text{prec}} \sim |1/T_c^M - 1/T_c^{\text{GR}}|^{-1}$. In the limit where $T_c^{\text{prec}} = T_c^M$, the RR relaxation timescale is $T_{\text{RR}}^M(a) \sim QP(a)$ (Equation 4).

SRR is to be contrasted with the residual torques that arise on timescales much longer than T_c^{prec} , when the orbital rosettes can be averaged over the precession period and conceptualized as concentric mass annuli. On those longer timescales, the residual torque on a test annulus due to the Poisson fluctuations in the orbital orientations of the finite number of background annuli has, by symmetry, only a transverse component. This changes the test annulus orientation but not the rosette’s eccentricity (j). This restricted form of RR is called vector RR (VRR), and its coherence time is set by self-quenching. By its definition (Equation 4), $T_{\text{RR}}^{\text{SQ}} \sim T_c^{\text{SQ}} \sim QP(a)/\sqrt{N_*(a)}$; i.e., the self-quenching coherence time is similar to the time it takes the orbital orientations to reach maximum randomization.

2.3. A General Framework for Describing Relaxation

Relaxation around an MBH can be described more generally in terms of a hierarchy of coherence times, averaged and conserved quantities, and effective particles and symmetries (**Table 1**;

Bar-Or & Alexander 2016). The general picture is that for progressively slower coherence-breaking mechanisms (the hierarchy: impulse→in-plane precession→self-quenching torques) and correspondingly longer coherence times ($T_c^{\text{NR}} \rightarrow [T_c^{\text{M}}, T_c^{\text{GR}}] \rightarrow T_c^{\text{SQ}}$), there are more periodic degrees of freedom in the problem that can be averaged out (none→mean anomaly→angle of periapse). From each of these emerges another conserved orbital quantity (none→ E → J). With each successive averaging, the symmetry of the effective particle grows (points→wires→annuli), and therefore the number of the remaining “torquable” degrees of freedom decreases, and the resonant torques on it decrease in magnitude. However, this decrease in τ_N is only by an order unity factor, whereas the coherence time T_c increases with symmetry as some power of N_* , which is a very large number. Therefore, the net result is that the relaxation timescales $T_{\text{RR}} \propto 1/(\tau_N^2 T_c)$ decrease with higher symmetry ($T_{\text{NR}} > T_{\text{RR}}^s > T_{\text{RR}}^v$).

Noncoherent two-body relaxation fits naturally in this framework as the limiting case of minimal symmetry, shortest coherence time, and longest relaxation timescale. NR is treated in the impulsive limit, where the interaction is effectively limited to the short flyby that lasts much less than the orbital time. For that reason, no averaging is possible and there are no conserved orbital quantities in the test orbit—NR can change any of them.

This hierarchy of relaxation timescales can have observable consequences. **Figure 3** shows the run with a of the various relaxation times in the Galactic Center, which suggests that RR plays a role in establishing some of the systematic trends observed in the different stellar populations there (Hopman & Alexander 2006).

Some of these theoretical insights into the nature of relaxation around an MBH were verified by direct N -body simulations (e.g., Eilon et al. 2009). However, a full-scale N -body simulation that spans the large dynamical and temporal range in the singular potential of the MBH is extremely challenging and still impractical. Even N -wire simulations (Touma et al. 2009), which evolve in time the phase-averaged wires directly, remain computationally expensive. One feasible method is to recast RR in terms of effective diffusion coefficients, and use Monte Carlo simulations to evolve test stars in phase space and statistically derive the stellar DF (Section 3.2.2).

3. DYNAMICS OF CLOSE MBH-STAR ENCOUNTERS

3.1. The Newtonian Loss Cone

A star on a nearly zero-energy (parabolic) orbit $E = GM_\bullet/2a \sim 0$ (note stellar dynamical inverse sign convention $E > 0$ for bound orbits) has eccentricity $e \rightarrow 1$, velocity $v(r) \simeq \sqrt{2GM_\bullet/r}$, specific angular momentum $J = \sqrt{GM_\bullet a(1-e^2)} = rv \sin \theta$ relative to the MBH, and a Keplerian periapse $r_p \simeq J^2/2GM_\bullet$. The proximity to the MBH can lead to prompt stellar destruction if r_p lies inside the event horizon or inside the tidal disruption radius. A star at distance r from the MBH has a periapse $\leq r_p$ if its velocity vector \mathbf{v} lies inside a cone centered on $-\mathbf{r}$, with an opening angle of $\sin \theta \simeq \sqrt{r_p/r}$. Generalizing to bound, nonzero energy orbits, the loss cone is the phase-space volume of orbits with $J(E) \leq J_{\text{lc}}(r_d) \simeq \sqrt{(2 - r_d/a)2GM_\bullet r_d}$, where r_d is the maximal periapse for destruction. In terms of the circular angular momentum $J_c = \sqrt{GM_\bullet a}$, $j_{\text{lc}} = J_{\text{lc}}/J_c = \sqrt{(2 - r_d/a)r_d/a} = \sqrt{1 - e_{\text{lc}}^2}$ (cf. **Figure 4a**). The phase-space volume of the loss cone is very small. For example, in a galactic nucleus similar to the Milky Way ($M_\bullet = 4 \times 10^6 M_\odot$, $r_h \sim 3$ pc), the angular size of the loss cone for the tidal disruption of $1-M_\odot$ MS stars at $r \sim r_h$ is $\theta_{\text{lc}} \sim \sqrt{r_p/r_h} \sim 10^{-3}$ rad (Section 4). This corresponds to a fraction of $\theta_{\text{lc}}^2/4$ of the stars at r_h (assuming an isotropic stellar distribution) or $Q\theta_{\text{lc}}^2/4 \sim \mathcal{O}(1)$ stars on a loss-cone orbit. Because such stars are promptly destroyed in less than an orbital period, the steady-state rate of TDEs is set by the processes that repopulate the loss cone.

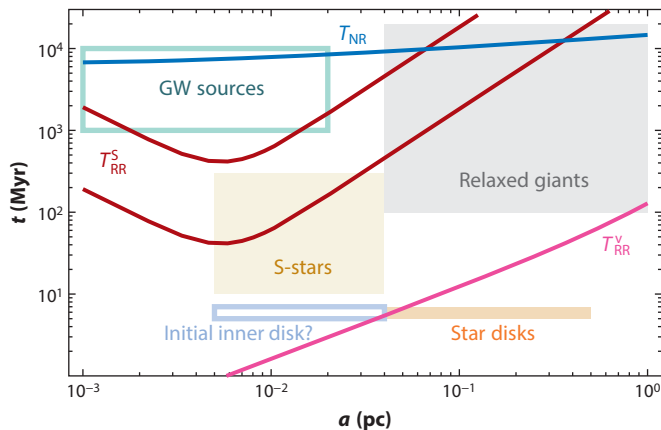


Figure 3

The relaxation timescales in the Milky Way’s nucleus near the 4×10^6 - M_\odot MBH, shown against the typical ages of various stellar populations there, assuming a relaxed stellar cusp (Hopman & Alexander 2006). The NR time T_{NR} (blue line) is nearly constant and only somewhat shorter than $t_{\text{H}} \sim 10$ Gyr (e.g., Preto & Amaro-Seoane 2010). Scalar RR of J , on timescale T_{RR}^{S} (red line) is shown for an assumed mean background stellar mass of $\langle M_\star \rangle = 1 M_\odot$ (upper red line), and $\langle M_\star \rangle = 10 M_\odot$ (lower red line) (simplified by assuming a J -averaged T_{c}^{GR} , an early approximation that is now superseded by the η -formalism; see Section 3.2.2). T_{RR}^{S} is shortest on the $\mathcal{O}(0.01)$ pc scale, where stellar mass BHs accumulate by mass segregation (Section 2.1.4) and are eventually driven to orbital decay by the emission of GWs (Section 5). Closer to the MBH, scalar RR becomes inefficient due to quenching of RR by rapid prograde GR precession and further away by quenching due to retrograde mass precession (Section 2.2). It is noteworthy that the red giants appear dynamically relaxed (Genzel et al. 2000) despite the fact that a large fraction of them are shorter lived than either stellar NR or scalar RR. This may be a hint that additional relaxation mechanisms are at work (Section 2.1.3). Vector RR of the orbital plane, on timescale T_{RR}^{V} , is much faster (magenta line) and could be the mechanism responsible for the inner truncation of the observed stellar disk. Both scalar and vector RR may explain the randomization of the S-stars (a cluster of MS B stars) that orbit the inner few $\times 0.01$ pc of the Galactic Center (Section 1.4). Abbreviations: BH, black hole; GR, general relativity; GW, gravitational wave; MBH, massive black hole; MS, main sequence; NR, nonresonant (two-body) relaxation; RR, resonant relaxation.

3.1.1. E versus J diffusion. Diffusion into the loss cone is characterized by a clear separation of scales. It is faster to reach the MBH by diffusion in J than in E . This property plays a crucial role in simplifying the analysis of loss-cone dynamics (Section 3.2.2). In the impulsive limit, two-body scatterings over a short time dt change only the velocity of the test particle, but not its position, and the change is isotropic and its rms small, $|\Delta \mathbf{v}| \ll v$. The specific kinetic energy of the test star $E = v^2/2$ then changes by $\Delta E \simeq \mathbf{v} \cdot \Delta \mathbf{v}$, and so $\Delta E/E \sim \Delta a/a \sim \mathcal{O}(\Delta v/v)$. Similarly, the specific angular momentum $J = |\mathbf{r} \times \mathbf{v}|$ changes by $\Delta J \simeq |\mathbf{r} \times \Delta \mathbf{v}|$, and so $\Delta J/J_{\text{c}} \sim \mathcal{O}(\Delta v/v)$, where $J_{\text{c}} \sim rv$. The relative (logarithmic) changes are therefore $\Delta \log E \sim \Delta \log a \sim \mathcal{O}(\Delta v/v)$ and $\Delta \log J \sim (\Delta J/J_{\text{c}})(J_{\text{c}}/J) \sim \mathcal{O}(\Delta v/v)/j$ (i.e., the diffusion velocity in $\log J$ is $1/j$ times faster than in $\log E$). Orbits that are already somewhat eccentric evolve so much faster in J than E that E (and a) can be approximated as constant. The relaxation time for diffusing into the loss cone is $T_J = J^2/D_{JJ} \sim j^2 T_E$ (Figure 4). Moreover, the logarithmic distance to the innermost stable orbit in the a direction is longer than it is in the J direction. The innermost stable circular orbit (ISCO) of a nonspinning MBH is at $a_\bullet = 6r_{\text{g}}$, whereas the lowest stable angular momentum for a parabolic orbit (a good approximation for plunge orbits) is $J_\bullet = 4r_{\text{g}}c$. Therefore, the logarithmic distances to the MBH from an initial orbit at (a_0, J_0) are $\Delta_a = \log(a_0/6r_{\text{g}})$ and $\Delta_J = \frac{1}{2} \log(j_0^2 a_0/16r_{\text{g}})$, where $j_0 = J_0/J_{\text{c}}(a_0)$, and their ratio is $\Delta_a/\Delta_J = 2[\log(a_0/r_{\text{g}}) - \log 6]/[\log(a_0/r_{\text{g}}) - \log 16 + \log(j_0^2)] > 2$.

ISCO: innermost stable circular orbit

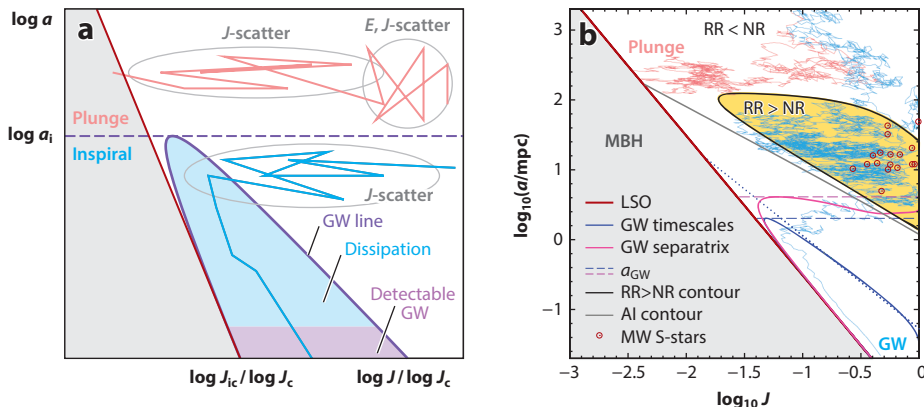


Figure 4

(a) A schematic of loss-cone dynamics in (a, j) phase space. At $J \lesssim J_c$ the scattering rates in $\log a = -\log E$ and $\log J$ are comparable, but once $J \ll J_c$, the scattering along $\log J$ is much faster (Section 3.1.1). Close to the MBH all random trajectories along $\log J$ cross the GW line into a region where GW dissipation is faster than NR, and therefore they inspiral into the MBH with high probability. Above the tip of the GW line, at a critical $\text{sma } a_i$, all stars plunge directly into the MBH with high probability. (b) An exact calculation of the critical lines and regions for a model of the Milky Way with $Q = 4 \times 10^5$, mass-precession coherence time, and Gaussian noise (Bar-Or & Alexander 2016). Orbits in the gray area below the LSO (dark red line) are unstable and promptly plunge into the MBH event horizon (Monte Carlo-generated plunge track example shown as a light red line). Where RR diffusion is faster than NR diffusion (yellow region), RR dominates the dynamics. The S-stars observed near the MBH of the Milky Way (red circles) (Gillessen et al. 2009) lie in the RR-dominated region (Sections 1.4 and 2.2). AI suppresses RR torquing below the AI line (gray). Inside the phase-space region delimited by the GW line (blue), GW dissipation is faster than NR J -scattering, and orbits spiral into the MBH by the emission of GW (Monte Carlo-generated inspiral track example shown as a light blue line). The critical sma for EMRIs, $a_i = a_{\text{GW}}$ (thin black line), corresponds to the maximum of the GW curve; below it stars become EMRIs before they cross the last stable orbit line. The approximate power-law GW line with the often assumed simplification $j_{\text{lc}} \rightarrow 0$ (dotted blue line) substantially overestimates a_{GW} . The exact separatrix streamline (magenta line) provides a more accurate estimate of a_{GW} than either of the timescale-based GW lines. Abbreviations: AI, adiabatic invariance; EMRI, extreme mass-ratio inspiral; GW, gravitational wave; LSO, last stable orbit; MBH, massive black hole; NR, nonresonant (two-body) relaxation; RR, resonant relaxation; sma, semimajor axis.

In particular, $\Delta_a / \Delta_J \rightarrow \infty$ as $j_0 \rightarrow 0$. Because the velocity along the J direction is faster while the distance is shorter, diffusion into the loss cone is primarily in angular momentum.

3.1.2. Plunge versus inspiral. There are in general two dynamical modes by which objects fall into an MBH (Alexander & Hopman 2003). One is by direct plunge, as discussed above, where the object is promptly removed from the system once it approaches the MBH closer than some destruction radius r_d . The removal needn't involve actual destruction: For example, the tidal separation of a binary removes the binary but does not destroy its constituent stars (Section 4.4.1). The distinguishing trait of a plunge process is that the object is required to remain on the plunging orbit only long enough to pass through periaapse once, which is less than one orbital time. Plunging orbits occur in one of two dynamical regimes, defined by the ratio of the orbital period $P(a)$ to the relaxation time across the loss cone, $T_J(a) = j_{\text{lc}}^2 T_E(a)$: the empty and full loss-cone regimes (Lightman & Shapiro 1977).

Close to the MBH, where $P(a)/T_J(a) < 1$, the star plunges almost unperturbed into the MBH, and the time-averaged phase-space density in the loss cone is nearly zero, because it takes slow

diffusion to supply new stars to plunge orbits. This is the empty, or diffusive, loss-cone regime. This regime extends up to a critical sma a_p , defined by $P(a_p)/T_J(a_p) = 1$. The total plunge rate from the empty loss-cone regime is approximately (Bar-Or & Alexander 2016)

$$\Gamma_p(a_p) \approx \frac{5}{32} \frac{N_*(< a_p)}{\log[1/j_{lc}(a_p)] T_E(a_p)} = 10 \frac{\log Q}{\log[1/j_{lc}(a_p)]} \frac{N_*^2(< a_p)}{Q^2 P(a_p)}, \quad (5)$$

where T_E is expressed in terms of the system parameters by Equation 2 and where a single mass Bahcall–Wolf steady-state solution is assumed.

Far from the MBH, where $a > a_p$ and $P(a)/T_J(a) > 1$, stars are scattered in and out of the loss cone many times before they reach periaipse, and therefore the loss cone is full, and the stellar distribution is effectively isotropic. In the full loss-cone regime, $\Gamma_p \sim j_{lc}^2 N_*/P$. Analysis of the relative contributions to the plunge rate from the empty and full loss-cone regimes around an MBH shows that most of the plunging stars come from $a_e \sim \min(a_p, r_h)$ and that the empty loss-cone rate (Equation 5) provides a reasonable approximation for the total rate from both regimes with the substitution $a_p \rightarrow a_e$ (Lightman & Shapiro 1977, Syer & Ulmer 1999), which for $M_\bullet \gtrsim 10^6 M_\odot$, where $a_p > r_h$, yields $\Gamma_p \sim \mathcal{O}(1/P_h)$ (Equation 1).

The second mode of getting to the MBH is by inspiral, where the orbit decays gradually by some dissipation mechanism that extracts a small fraction of the orbital energy and angular momentum every orbit until the orbit shrinks below the ISCO. The dissipation mechanisms of interest, GW emission (Section 5.1), tidal heat dissipation (Section 4.2.4), or hydrodynamical interaction with a massive accretion disk (Section 7), are typically strongly decreasing functions of radius, and so most of the orbital energy is extracted near periaipse.

In contrast to prompt plunge, inspiral down to the ISCO is gradual and takes many orbital times, during which the orbit is susceptible to perturbations by the background stars. These can abort the inspiral before the star reaches the MBH, either by deflecting it to a lower eccentricity and larger periaipse orbit, where dissipation is inefficient, or by deflecting it directly to a plunge orbit. The total time for inspiral increases with the initial sma. The race between inspiral and orbital diffusion limits inspiral to stars that begin the process close enough to the MBH so that the total inspiral time is faster than the relaxation time. Phase space is therefore separated into two regimes, which are approximately described by a critical sma for inspiral, a_i (**Figure 4**). At $a > a_i$, stars that reach the MBH do it with high probability by direct plunge, whereas at $a < a_i$ they do it with high probability by inspiraling into it. The transition between the two regimes is quite sharp (Hopman & Alexander 2005). There is no full loss-cone regime analogue for inspiral events. The total inspiral rate can be approximated by (Alexander & Hopman 2003, Bar-Or & Alexander 2016)

$$\Gamma_i \approx \Gamma_p(a_i) \sim (a_i/r_h) \Gamma_p(r_h), \quad (6)$$

where the last approximate relation neglects the logarithmic diffusion terms and assumes $\alpha = 7/4$. Because the inspiral time is much longer than the time to plunge, $a_i \ll r_h$ and the inspiral rate is much lower than the plunge rate. This simply reflects the fact that there are many more stars inside r_h , which can diffuse to plunge orbits, than there are stars inside a_i , which can diffuse to inspiral orbits. For example, for a Milky Way–like nucleus, where $r_h \sim \text{few} \times 1 \text{ pc}$ and $a_i \sim \text{few} \times 0.01 \text{ pc}$ (Hopman & Alexander 2005), the ratio of GW inspiral rate to plunge rate⁹ is $\Gamma_i/\Gamma_p \sim \mathcal{O}(0.01)$.

⁹This is considered in the Newtonian loss-cone context, in spite of the inclusion of GW dissipation, because any type of dissipation can be represented by the inspiral formalism, but the nondissipative dynamics are approximated as Newtonian (Section 3.1.3).

3.1.3. Resonant relaxation in the Newtonian limit. Early studies of the loss-cone problem (Frank & Rees 1976, Lightman & Shapiro 1977, Shapiro & Marchant 1978) were confined to the Newtonian limit and did not include RR, which was not yet discovered. Nevertheless, the consequences of this omission for global loss-rate estimates turn out to be small, due to a coincidence that can be fully explained only in the context of the relativistic loss cone (Section 3.2). RR does not affect the plunge rates much, because most plunges originate at $a \sim r_h$, where mass precession quenches scalar RR (Section 2.2; **Figure 3**). The relative contribution from the fewer stars closer to the MBH, where RR is dynamically important, is small (Rauch & Tremaine 1996). In contrast, the branching ratio between inspiral and plunge events, if treated in the Newtonian limit, appears to be dramatically (but incorrectly) affected by RR. This is because in the absence of GR Schwarzschild precession, the RR torques remain strong even on low- J orbits, and all stars evolve rapidly in J and plunge into the MBH before they can diffuse below a_i and inspiral into the MBH (Hopman & Alexander 2006, Bar-Or & Alexander 2016). As a result, the inspiral rate drops to zero. It is only when both the nondissipative (precession) and dissipative (GW) GR terms are included in the dynamics self-consistently that the quenching effect of GR precession is found to strongly limit the role of RR for the loss rates (**Figure 4b**). The bottom line is that the naive treatment of the loss-cone problem in the Newtonian limit, which neglects both GR dynamics (apart for the GW dissipation) and RR (in spite of the fact that it is a Newtonian process), yields by coincidence the correct order of magnitude for the plunge and inspiral rates (Section 3.2.3).

3.2. The Relativistic Loss Cone

The extension of the essentially Newtonian treatment of loss-cone dynamics (notwithstanding the GW dissipation term) to the relativistic regime was made necessary by the early realization that fast GR precession of an eccentric test star will rapidly switch the sign of the residual torques exerted on it by the nearly fixed background and quench RR (Rauch & Tremaine 1996). This has important implications for EMRIs. Hopman & Alexander (2006) conjectured that GR precession could prevent RR from pushing all potential EMRI sources into prompt plunge trajectories, because the $\mathcal{O}(\beta^2 j^{-2})$ GR precession becomes significant before $\mathcal{O}(\beta^5 j^{-7} Q^{-1})$ GW dissipation (Alexander 2015). This would decouple the sources from the background and allow them to inspiral gradually and produce detectable quasi-periodic GW signals. This departure from the simplifying assumption that the test star is statistically similar to the background (Section 2.2) was treated in those early studies as equivalent to assuming that the background is precessing randomly relative to the test star; that is, GR precession was introduced as a stochastic perturbation of the background stars (Rauch & Tremaine 1996).

3.2.1. The Schwarzschild barrier. The first self-consistent post-Newtonian N -body simulations of plunge and inspiral events (Merritt et al. 2011) indicated that GR precession is not well described that way and, in particular, that the coherent behavior of RR cannot be approximated by a Markov process. Not only did GR precession quench RR before the stars entered the GW-dominated regime, as conjectured, but the stellar trajectories seemed to encounter a barrier in phase space (the so-called Schwarzschild barrier, SB) that prevented them from evolving to $j \rightarrow 0$ and plunging or inspiraling into the MBH (cf. **Figure 5a**). Instead, the stars appeared to linger near the barrier for roughly T_c while their orbital parameters oscillated at the Schwarzschild precession frequency. An early analysis suggested that this behavior was related to precession under the influence of a residual dipole-like force (Alexander 2010, Merritt et al. 2011). Larger-scale N -body simulations confirmed that GR quenches RR near the SB (Brem et al. 2014). However,

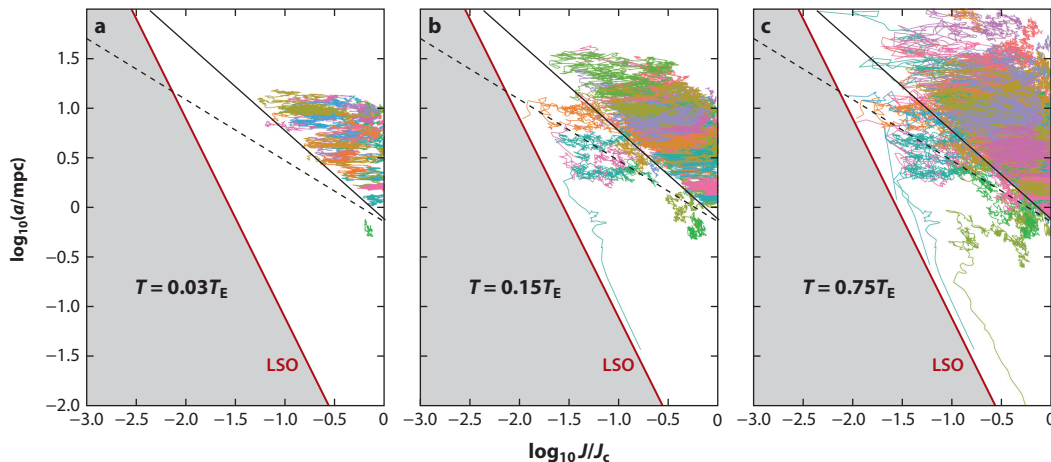


Figure 5

Snapshots of stellar tracks from a Monte Carlo integration of the FP equation describing orbital evolution around an MBH under the combined effects of NR, RR, and GW emission (Bar-Or & Alexander 2016). The snapshots (differently colored lines for each stellar track) are shown at increasing fractions of T_E , the NR energy diffusion time. The phase space is marked as in **Figure 4**, but for simplicity only the AI locus [solid black line at $j_{AI}(a) = \sqrt{T_c(a)/P_{GR}^0(a)}$] and the initially misidentified SB locus of Merritt et al. (2011) (dashed black line) are shown. It is now understood that the SB effect is due to AI (Bar-Or & Alexander 2014). On short timescales (panel *a*), stellar orbits evolve rapidly in angular momentum due to RR but only above the AI locus, because beneath it RR is strongly suppressed. However, on longer timescales NR randomizes the orbits, the AI barrier is breached, and the phase-space density approaches the maximal entropy solution (panel *b*). Abbreviations: AI, adiabatic invariance; FP, Fokker–Planck (equation); GW, gravitational wave; MBH, massive black hole; NR, nonresonant (two-body) relaxation; RR, resonant relaxation; SB, Schwarzschild barrier.

the exact nature of the SB and the interpretation of stellar dynamics near it remained controversial (e.g., Antonini & Merritt 2013).

3.2.2. The η -formalism. The SB phenomenon lies in the difficult-to-treat interface between deterministic Hamiltonian dynamics and stochastic kinetic theory. The η -formalism (Bar-Or & Alexander 2014) provides a formal framework for describing coherent relaxation and secular processes around an MBH, and it succeeds in explaining the SB phenomenology that is observed in N -body simulations (**Figure 5**) and in reproducing the N -body loss rates (Bar-Or & Alexander 2016).

The key idea of the η -formalism is that the effect of the background stars on the test orbit can be represented as a time-correlated noise model.¹⁰ A perturbative expansion of the phase-averaged post-Newtonian Hamiltonian reveals that to leading order, the noise is a vector in angular momentum phase space, $\eta(t)$. The noise model is characterized by an autocorrelation function with a coherence timescale T_c . Stochastic equations of motion are then derived from the Hamiltonian and used, together with random realizations of correlated noise, to evolve test orbits in phase space. The resulting dynamics are found to depend critically on the temporal smoothness (degree of differentiability) of the noise. When the noise is smooth (infinitely differentiable, as expected for noise generated by the superposition of many smooth background orbits), its power

¹⁰The noise can be approximated as independent of J (i.e., fully correlated in J), because the mean free path in J is small: $\tau_N T_c^M \ll J_c$ (Section 2.2) and $\tau_N T_c^{SQ} < J_c$ (Kocsis & Tremaine 2015).

spectrum drops fast beyond some maximal frequency. A star precessing faster than that cutoff frequency is effectively decoupled from the perturbing background by AI. For GR precession, the AI/SB barrier in phase space is the locus [Equation 7 (Bar-Or & Alexander 2014) corrects the SB's misidentified locus of Merritt et al. (2011)]

$$j_{\text{AI}}(a) \simeq \sqrt{T_c(a)/P_{\text{GR}}^0(a)}, \quad (7)$$

where $P_{\text{GR}}^0 = (a/3r_g)P$ is the GR precession period for $j = 1$.

Although the noise is correlated, it is possible to derive (and validate against results from the stochastic equations of motion) effective diffusion coefficients,¹¹ which allow one to evolve the probability density function $\rho(j)$ with the FP equation.¹² The RR diffusion coefficient $D_{jj}^{\text{RR}}(j; a)$ is proportional to the power spectrum of the noise at the precession frequency $\nu_{\text{GR}}(j; a) = 2\pi/P_{\text{GR}}^0(a)j^2$, and therefore for smooth noise models, AI is manifested as an extremely steep fall in the RR diffusion rate for $j < j_{\text{AI}}(a)$. The AI/SB barrier is not a reflecting barrier but a locus in phase space beyond which only NR diffusion is effective. RR diffusion beyond the AI/SB barrier does not fall to zero identically. Because diffusion to yet lower j slows further down, whereas diffusion to higher j speeds further up, orbits seem statistically to bounce away from the SB back to higher j . The highly suppressed but nonzero RR diffusion beyond the barrier means that the zero-density front advances to lower j logarithmically slowly in time. However, for practical purposes the barrier can be considered fixed.

The ability to implement the η -formalism of RR as diffusion is of great practical value. It allows us to model the dynamics of galactic nuclei in the $N_* \rightarrow \infty$ limit by evolving the probability density via Monte Carlo simulations of the combined NR and RR diffusion, including additional processes such as GW decay¹³ (Bar-Or & Alexander 2016).

3.2.3. Steady-state phase-space structure and loss rates. The η -formalism does not take into account diffusion by NR, which is unaffected by precession (Section 2.3), and continues independently across phase space. **Figure 4b** shows the region in phase space where the RR diffusion rate is faster than NR and the locus of the AI line, below which the RR diffusion rate is essentially zero. The RR-dominated region is separated from the loss lines (plunge and GW inspiral), and therefore the bottleneck for the loss rates remains slow NR, with only a modest boost from RR (Section 3.1.3). On timescales $\mathcal{O}(T_E)$, NR erases the density drop beyond the AI/SB barrier, and the system rapidly approaches the maximal entropy configuration (**Figure 5**), as it should, irrespective of the nature of the randomization process. However, the existence of an RR-dominated region in phase space may play an important role in the orbital evolution of special populations in galactic nuclei, e.g., the S-stars in the Galactic Center (Sections 1.4 and 4.4.1).

Figure 6 shows the plunge and inspiral rates per galaxy, as a function of M_* , that were estimated by Monte Carlo simulations that used NR and effective RR diffusion coefficients to evolve test stars in phase space (M_*/σ with $\beta = 4$ assumed). The results confirm and calibrate the weak approximate

¹¹General maximal entropy considerations fix the steady-state J -DF for J -evolution under RR. The FP equation then imposes a relation (the fluctuation-dissipation relation; Callen & Welton 1951) that must be satisfied by any valid RR diffusion coefficients.

¹² $\partial\rho/\partial t = \frac{1}{2} \frac{\partial}{\partial j} \{j D_{jj} \frac{\partial}{\partial j} (\rho/j)\}$ with a parametric drift coefficient $D_j = \frac{1}{2j} \frac{\partial}{\partial j} (j D_{jj})$.

¹³The NR+RR+GW FP equation is evolved in time by Monte Carlo simulations by incrementing the test star's phase-space position in dimensionless energy and angular momentum (ϵ, j) over a small time interval dt using the NR and RR diffusion coefficients and approximations for the energy and angular momentum dissipation by GW over dt , $d\epsilon^{\text{GW}}$ and dj^{GW} : $d\epsilon = D_\epsilon^{\text{NR}} dt + \gamma_1 \sqrt{D_{\epsilon\epsilon}^{\text{NR}}} dt + d\epsilon^{\text{GW}}$ and $dj = D_j^{\text{NR}} dt + \gamma_2 \sqrt{D_{jj}^{\text{NR}}} dt + D_j^{\text{RR}} dt + \gamma_3 \sqrt{D_{jj}^{\text{RR}}} dt + dj^{\text{GW}}$, where γ_1, γ_2 , and γ_3 are randomly drawn normal variates, with γ_1 and γ_2 correlated with a correlation coefficient $\xi = D_{\epsilon j} / \sqrt{D_{\epsilon\epsilon} D_{jj}}$.

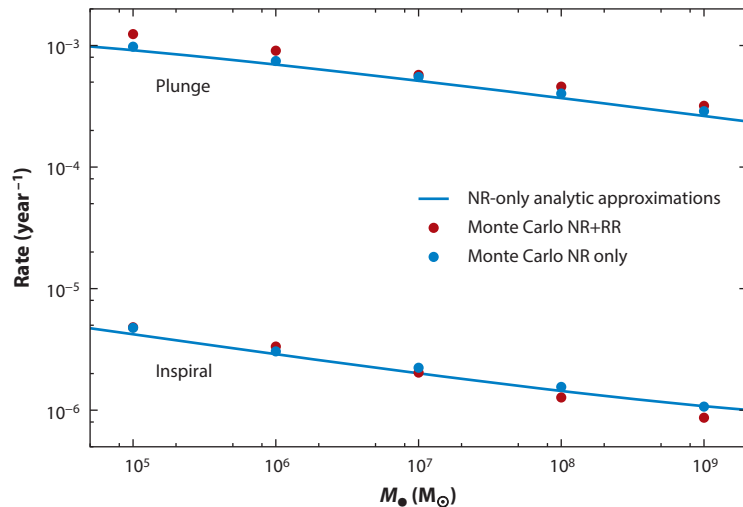


Figure 6

Plunge and EMRI rates per galaxy in steady state, as a function of M_\bullet , assuming a simplified single mass population composed of $10\text{-}M_\odot$ stars (stellar BHs), scaled to the Galactic Center by the M_\bullet/σ relation with $\beta = 4$. The rates were estimated by Monte Carlo simulations that implement the η -formalism (Section 3.2.2) (circles) and are compared with NR-only analytic approximations (lines) (adapted from Bar-Or & Alexander 2016). The analytic estimates match the corresponding NR-only Monte Carlo simulations well and deviate only slightly from the full NR+RR simulations (Section 3.2.3). The plunge rates are evaluated in the empty loss-cone limit, which gradually overestimates the true rate below $M_\bullet \lesssim 10^6 M_\odot$, where $a_p < r_h$ (Section 3.1.2). Abbreviations: BH, black hole; EMRI, extreme mass-ratio inspiral; NR, nonresonant (two-body) relaxation; RR, resonant relaxation.

$M_\bullet^{-1/4}$ dependence of the rates (Hopman 2009b). The close similarity between the rates with and without RR shows that the strong suppression of RR below the AI line indeed decouples the EMRIs from the background, and allows them to proceed unimpeded, as conjectured (Hopman & Alexander 2006).

3.2.4. Other approaches to modeling dynamics near an MBH. Dynamics near an MBH involve many processes, including NR, RR, and secular Newtonian and GR processes. Direct relativistic N -body simulations (with either full or perturbative GR) (Merritt et al. 2011, Brem et al. 2014) generate by construction all these processes. However, the interpretation of the results is very difficult because these complex dynamics are entangled. Moreover, special regularization techniques are required for maintaining high numeric accuracy over the large dynamical range in the diverging potential of the central mass (e.g., Mikkola & Merritt 2006). These are very expensive computationally, and limit the simulations to unrealistically small N_\star , which generally cannot be scaled up to astrophysically relevant values because different dynamical mechanisms scale differently with N_\star (e.g., Heggie & Hut 2003).

Because most of the questions of interest in the modeling of processes near an MBH involve integration over timescales much longer than an orbital period, one alternative to direct N -body simulations is “ N -wire” simulations (Touma et al. 2009), which treats the dynamics directly in terms of the orbit-averaged mass wires (Section 2.2) with time steps $> P$. Unfortunately, the computational load of each time step is currently still too heavy to provide clear advantage over direct N -body simulations.

A recent attempt to derive a self-consistent description of the background noise and its correlations from the Balescu–Lenard master equation may ultimately provide an ab initio description of the noise (Fouvry et al. 2016). However, the feasibility of its adaptation to practical applications remains to be proven.

3.3. Noncollisional Loss-Cone Refilling

The angular momentum J is an integral of motion in spherical potentials, and therefore collisions (NR or RR) are necessary for refilling the loss cone with stars on $J < J_{lc}$ orbits. In nonspherical potentials this is no longer the case, and the angular momentum of individual orbits can change over time, whether in a restricted J range or in an unrestricted one that includes $J = 0$ (e.g., chaotic orbits in a triaxial potential). When the range includes $J \rightarrow 0$, the orbits are called centrophilic. Stars on such families of orbits can be driven into the loss cone by collisionless torques, until the entire reservoir is “drained” (Vasiliev & Merritt 2013; see the review by Vasiliev 2014). The time for collisionless torquing to push a star into the loss cone is generally much shorter than NR diffusion, and as long as the supply of centrophilic orbits holds, the loss rate reaches, or even surpasses, the maximal rate of collisional loss-cone refilling, which is given by the full loss-cone rate (Section 3.1.2). Even after the reservoir is drained, the lowered symmetries of galactic potentials that allow collisionless torquing of centrophilic orbits effectively increase the loss cone, because slow relaxation now needs only to refill the larger phase space of centrophilic orbits, and the collisionless torques will rapidly take the stars on to the loss cone.

This is what is found for axisymmetric galaxies (Magorrian & Tremaine 1999), where the draining phase is cosmologically brief and can therefore be neglected. The lowered symmetry indeed expands the loss cone into a larger “loss wedge,” but the steady-state increase in the plunge rate is only by about a factor of two. The situation is different for triaxial galaxies, where the draining time can be longer than t_H , and the loss cone is not in steady state. In that case, the question whether collisionless torquing dominates loss-cone dynamics directly reflects assumptions about the initial conditions: What was the initial mix of orbital families and what was the initial distribution of angular momentum? An additional uncertainty is due to orbital scattering by the MBH, which may drive the stellar potential near it to isotropy (Gerhard & Binney 1985). The role of noncollisional loss-cone refilling in the cosmic loss rates remains unclear.

4. TIDAL INTERACTIONS BETWEEN STARS AND AN MBH

A disruptive tidal interaction occurs when a star (or binary or gas cloud) of mass M_* and radius R_* approaches the MBH on an orbit with periape $r_p < r_t = Q^{1/3} R_*$. The work done by the tidal field transfers energy and angular momentum from the orbit to the star and unbinds it. In the case of a nondisruptive impulsive tidal interaction, such as a hyperbolic flyby with $r_p \gtrsim r_t$, or an eccentric periodic orbit with $a \gg r_p \gtrsim r_t$, the strong tides excite oscillations in the star, and possibly also lead to some mass loss, but the star survives (Section 4.2.4).

4.1. Classification of Tidal Disruptions

The characteristics of a tidal interaction with a BH, and the physical processes that are required to describe it, depend on three length scales: the stellar radius, R_* ; the tidal radius, r_t ; and the gravitational radius of the BH, r_g . Their ratios can be expressed in terms of the stellar break-up velocity, v_* , which measures the star’s self-gravity, and in hydrostatic equilibrium, also its

pressure: $r_t/R_\star = Q^{1/3}$, $r_t/r_g = (v_\star/c)^{-2} Q^{-2/3}$, and $r_g/R_\star = (v_\star/c)^2 Q$. There are generally five full disruption regimes, ordered by the mass ratio Q (Alexander 2005).

1. $Q \ll 1$ ($r_g \ll r_t \ll R_\star$): A weak Newtonian tidal interaction, where the star's self-gravity and pressure dominate. Relevant when a stellar BH is swallowed by a star and can result in an exotic star powered by accretion (e.g., Thorne & Zytkov 1975).
2. $Q \sim 1$ ($r_g \ll r_t \sim R_\star$): A strong Newtonian tidal interaction with significant mass loss and possible disruption, such as occurs in a close interaction between a stellar BH and a massive star (Section 4.4.2).
3. $Q \sim (c/v_\star)^2$ ($R_\star \sim r_g < r_t$): A complete disruption in the Newtonian regime, as would be the case for disruption by an IMBH.
4. $(c/v_\star)^2 < Q < (c/v_\star)^3$ ($R_\star \ll r_g < r_t$): A complete tidal disruption by a lower-mass MBH of the type considered here (e.g., Sgr A*), which can be treated as Newtonian to a good approximation (the subsequent circularization and accretion of the debris are in the relativistic regime).
5. $Q > (c/v_\star)^3$ ($R_\star \ll r_t \ll r_g$): Tidal disruption inside the event horizon. The star plunges into the MBH as a point particle on a GR trajectory.

4.2. Stellar Disruption

TDEs can be an important mass supply channel for lower-mass MBHs. This is seen by comparing the plunge rate $\Gamma_t \propto \dot{M}_\bullet^{-1/4}$ (Figure 6) to the MBH mass, approximating a constant rate over t_H and $M_\star \sim 1 M_\odot$, which yields $\dot{M}_\bullet \sim M_\star \Gamma_t t_H$ for $\dot{M}_\bullet \lesssim 10^7 M_\odot$ (simulations indicate that the TDE contribution is $(0.15-0.65)\dot{M}_\bullet$; Murphy et al. 1991, Freitag & Benz 2002). For such lower-mass MBHs $r_t > R_\star$, and therefore the accretion of stars is luminous. Tidal accretion flares can signal the presence of an otherwise quiescent growing MBH and probe accretion physics.

4.2.1. Physics of stellar disruption. The disrupted star is typically scattered into the loss cone from a long-period orbit with $a \sim r_h$ (Section 3.1.2) and is therefore on a hyperbolic orbit relative to the MBH, with specific orbital energy ϵ that is a small fraction of its binding energy $\epsilon_\star = -v_\star^2$, $\epsilon \sim \mathcal{O}(0.1)|\epsilon_\star|$ (e.g., Alexander & Livio 2001). The orbit can therefore be approximated as parabolic ($\epsilon = 0$). The work done by the tidal field on the star transfers orbital energy $\Delta\epsilon \sim GM_\bullet R_\star/r_t^2 \sim Q^{1/3}\epsilon_\star \gg \epsilon_\star$ to it, thereby disrupting the star.¹⁴ Roughly half the stellar debris is ejected to infinity with positive orbital energy up to $\epsilon_{\text{out}} \sim \epsilon_\star + \Delta\epsilon \sim +\Delta\epsilon$, whereas the other half is captured with negative orbital energy down to $\epsilon_{\text{in}} \sim \epsilon_\star - \Delta\epsilon \sim -\Delta\epsilon$. The most bound debris stream returns to the point of disruption near the MBH on an eccentric orbit after time $t_{\text{min}} = (\pi/\sqrt{2})Q^{1/2}t_\star$. The rest of the bound mass follows with a decreasing fallback rate $\dot{M}_{\text{fb}} = \dot{M}_\star/(3t_{\text{min}})(t/t_{\text{min}})^{-5/3}$ [Rees 1988; note that this relation originally appeared in Rees (1988) with a known typo ($t^{-4/3}$)]. The peak fallback rate $\max \dot{M}_{\text{fb}} = \dot{M}_\star/(3t_{\text{min}})$ exceeds the Eddington limit for $\dot{M}_\bullet \lesssim 3 \times 10^7 M_\odot$. Note that the connection between the mass fallback rate and the observable accretion emission is neither direct nor obvious, because the gas must first circularize before luminous accretion can proceed, because it is not clear how the initial super-Eddington phase appears observationally and because the luminosity emitted at specific bands at different times is not simply proportional to \dot{M}_{fb} . Though theoretically unjustified, the $F_\nu \propto t^{-5/3}$ flux decline remains a conventional criterion for distinguishing tidal flares from other types of AGN activity.

¹⁴It was recently realized that $\Delta\epsilon$ hardly depends on the penetration depth $b = r_p/r_t$, because once the star crosses r_t , its self-gravity is negligible, and the tidal field no longer performs work against it (Sari et al. 2010, Guillochon & Ramirez-Ruiz 2013, Stone et al. 2013).

This simplified initial picture of TDEs was subsequently refined and modified. It is now understood that the early phases of the fallback (the rise and the settling on the asymptotic $t^{-5/3}$ decline) depend on the details of the stellar structure (Lodato et al. 2009). Partial tidal disruption leads to a faster than $t^{-5/3}$ decline, due to the fact that some of the tidal interaction's energy is transferred to the bound remnant at the expense of the debris (Guillochon & Ramirez-Ruiz 2013). GR precession and frame dragging appear to play a crucial role in the postdisruption circularization of the debris streams, especially if the orbit is bound (Dai et al. 2013), by misaligning debris streams of different energies and enhancing the shocks as they intersect near the disruption point (Guillochon & Ramirez-Ruiz 2015, Bonnerot et al. 2016, Hayasaki et al. 2016). GR precession may also link the penetration depth with the flare temperature, because deeper penetration leads to a larger precession angle and an intersection point deeper in the MBH potential (Dai et al. 2015).

4.2.2. Observed tidal disruption flares. More than 20 TDEs have been observed to date in the radio, optical, UV, X-ray, and γ -ray bands. This translates to a rate of $\sim 10^{-5} \text{ year}^{-1} \text{ gal}^{-1}$ (Stone & Metzger 2016). The predicted plunge rates shown in Figure 6 ($\sim 5 \times 10^{-4} \text{ year}^{-1} \text{ gal}^{-1}$ for $M_{\bullet} = 10^7 M_{\odot}$; Bar-Or & Alexander 2016) are in line¹⁵ with other predictions of $\Gamma_t \gtrsim 10^{-4} \text{ year}^{-1} \text{ gal}^{-1}$ (Magorrian et al. 1998, Wang & Merritt 2004), and they all are systematically above the observed rate by about a factor of ten (Stone & Metzger 2016). The meaning of this tension between the uncertain predicted rates and the observed ones is still unclear.

Recent observations indicate that TDEs are overrepresented in rare galaxies that exhibit signs of a recently ended (0.1–1 Gyr old) intense star-formation epoch (Arcavi et al. 2014), as evidenced by the strong presence of A-type stars.¹⁶ TDEs are overabundant in these poststarburst galaxies by factors of 33–190, and the implied TDE rate for this special class of hosts is $10^{-3} \text{ year}^{-1} \text{ gal}^{-1}$ (Stone & van Velzen 2016). This further exacerbates the discrepancy between the predicted and observed rates in all other galaxy types.

There are various possible explanations for the connection between poststarburst galaxies and elevated TDE rates. If the starburst is triggered by a recent galactic merger, a binary MBH in the center may increase the TDE rate by several orders of magnitude (Chen et al. 2011). However, this phase is too brief to explain more than $\mathcal{O}(0.01)$ of the overall high TDE rate (Wegg & Bode 2011), and furthermore it requires a coincidence between the decay times of binary MBHs and the life span of A stars. Alternatively, the high TDE rate may follow a dissipative flow of gas to the galactic nucleus that results in a central starburst and an unusually high central stellar density. This leads to a high TDE rate (if in steady state, $\Gamma_t \propto N_{\star}^2$; Equations 2 and 5). Observations of nearby A+E galaxy NGC 3156 indeed indicate a dense nucleus that can support a high TDE rate of $\Gamma_t \sim 10^{-3} \text{ year}^{-1}$ (Stone & Metzger 2016).

4.2.3. Tidal detonation. During a deep tidal encounter ($r_p/r_t \ll 1$), the ballistic trajectories of different mass elements in the disrupting star converge (“pancake”) to the orbital plane of the star’s center of mass and reach a transient state of high density, pressure, and temperature at periape

¹⁵These plunge rates (Bar-Or & Alexander 2016) are for horizon crossing, not tidal disruption. The adaptation of the calculations to tidal disruption involves substituting $J_{\text{lc}} = 4r_g c$ by $J_t = \sqrt{2GM_{\bullet}r_t}$ for an $e = 1$ marginal tidal disruption orbit. However, because $J_t/J_{\text{lc}} = \sqrt{r_t/8r_g} \simeq 2.4(M_{\bullet}/10^6 M_{\odot})^{-1/3} \sim \mathcal{O}(1)$ (Solar-type star assumed), and because the plunge rate is a weak function of $j_{\text{lc}} \ll 1$ (Equation 5), the horizon crossing rates are also reasonable estimates for the MS TDE rates.

¹⁶In a TDE sample of eight events, six are in a class of hosts (2.3×10^{-2} of all galaxies) that include quiescent galaxies with strong Balmer absorption lines, which is a signature of A stars; of those six, three are also in A+E galaxies (2×10^{-3} of all galaxies) (French et al. 2016).

(Carter & Luminet 1982). The maximal compression and the temperature depend sensitively on the hydrodynamics of the flow, which become relevant once the temperature rises enough that the ballistic speed becomes subsonic. Detailed simulations (Laguna et al. 1993) indicate that when $r_p/r_t \lesssim \mathcal{O}(0.1)$, the density and temperature reach high enough values, for a long enough time, to ignite runaway nuclear fusion in the stellar core material, if it is already evolved (or the star is a WD; Rosswog et al. 2009) and composed of fast-fusing heavier elements (e.g., Alexander 2005). GR precession of the gas streams further enhances the compression by leading to multiple density maxima. The unusually energetic radio/X-ray source Sgr A East in the Galactic Center may be the outcome of a tidal nuclear detonation event (Dearborn et al. 2005).

4.2.4. Tidal heating and inspiral. When a star is scattered to an eccentric orbit with periapse $r_t < r_p \lesssim 2r_t$, nondestructive tidal interactions on successive peripassages transfer orbital energy to internal oscillations, mostly at the fundamental frequency $\nu_* \sim \sqrt{GM_*/R_*^3} \gtrsim \sqrt{GM_*/r_p^3}$ (Press & Teukolsky 1977). These cascade by nonlinear mode coupling to higher frequencies and ultimately dissipate as heat.¹⁷ Possible orbit-oscillation runaway resonances are further suppressed by the random phase perturbations due to the stellar background (Alexander & Morris 2003). As the orbit decays and the star inspirals in, the heating rate grows until the star approaches its Eddington luminosity. This tidally powered transient source, a “squeezar” (Alexander & Morris 2003), is ultimately destroyed after $\mathcal{O}(10^5)$ years, either by radiatively evaporating itself (a hot squeezar that radiates the tidal heat) or by expanding beyond its Roche lobe until it is tidally destroyed (an adiabatic cold squeezar). The mean inspiral event rate by tidal heating is much smaller than the TDE rate, $\sim 0.05\Gamma_t$ (Section 3.1.2); the estimated mean number of squeezars around an Sgr A*-like MBH is ~ 0.1 –1.

4.3. Near Misses

The TDE rate is also roughly the rate of near misses ($r_t < r_p \lesssim \text{few} \times r_t$), because the cross section for an encounter with periapse $\leq r_p$ scales as r_p due to gravitational focusing. A non-negligible fraction of the stars inside the radius of influence of a lower-mass MBH (such as Sgr A*) have undergone a near-miss flyby. This is because TDEs provide a substantial fraction of the mass for such MBHs (Section 4.2), and the stellar mass inside $a \lesssim r_h$, where most plunges originate, is also $\mathcal{O}(M_*)$. A second consecutive nondestructive flyby is unlikely. Because the star’s sma is typically $a \sim r_h$ and its orbit lies between the empty and full loss-cone regimes (Section 3.1.2), it will likely be deflected off the plunging orbit by background stellar perturbations or miss the MBH due to its Brownian motion (Bahcall & Wolf 1977, Chatterjee et al. 2002, Merritt et al. 2007) relative to the cusp’s center of mass (Alexander & Livio 2001). Furthermore, because mass tidally lost from the stellar envelope and bound to the MBH adds positive energy to the surviving star, the new apoapsis could lie well beyond r_h (Manukian et al. 2013). Near misses can be important if a single strong tidal interaction with the MBH has long-lasting effects on the star.

4.3.1. Tidal scattering. A strong nondestructive tidal interaction with an MBH leads to extreme distortion, spin-up, mixing, and mass loss. Of these, high spin and mass loss have the longest-lasting effects. Shortly after flyby, on the thermal relaxation timescale, the star will be redder (Manukian et al. 2013). The long-term effect of high spin is hotter, more luminous stars with abundance

¹⁷In the absence of efficient dissipation, orbit/oscillation resonances and/or reverse energy and angular momentum transfer back to the orbit are possible (Novikov et al. 1992).

anomalies due to mixing. Such unusual populations are observed in the Galactic Center (Carr et al. 2000). Quantitative estimates predict that $\mathcal{O}(0.01)$ of the stars in the radius of influence of the Galactic Center have undergone a strong tidal scattering event (Alexander & Livio 2001, Manukian et al. 2013).

4.3.2. Tidal disruption and tidal stripping of red giants. Tidal interactions of red giants with an MBH differ from those of MS stars due to the core/envelope dichotomy of red giant structure. This enables near-miss flybys to tidally strip a substantial fraction of the extended envelope while preserving the burning core. Due to the large size of the giant, the fallback time is long, and the fallback rate, and hence the luminosity, is lower than for an MS star (MacLeod et al. 2012).

The gas streams ejected from a tidally disrupted object move initially on ballistic orbits through the thin gaseous medium surrounding the MBH. The debris streams from stripped red giants are less dense than those from MS stars, both because the giant envelope is thinner and because the larger tidal radius corresponds to more spread-out streams. The debris is therefore more susceptible to dissolution by the Kelvin–Helmholtz instability as it orbits through the ISM. This can further decrease or even completely throttle the fallback rate on the MBH and decrease the tidal flare luminosity (Bonnerot et al. 2016). It thus appears unlikely that quiescent MBHs with mass $M_{\bullet} > 10^8 M_{\odot}$, which only disrupt giants, will reveal themselves by tidal flares. The cloud G2, which is tidally interacting with Sgr A* (Gillessen et al. 2012; Section 1.4), may be a clump in a debris stream of a recent tidal stripping event (Guillochon et al. 2014).

4.4. Three-Body Exchange Interactions

There are two variants of three-body exchange interactions with the MBH, which involve two stars and the gravitational separation of a bound two-body system. One is the interaction of an incoming stellar binary with a nearly radial unbound orbit with the tidal field of the MBH. Such interactions can lead to a separation of the binary, where one of its stars becomes bound to the MBH and the other is ejected as a single star (Section 4.4.1). The other possible exchange interaction occurs when a single incoming star on a nearly radial unbound orbit interacts with a binary system composed of the MBH and one of the stars closely bound to it. Such an interaction can also lead to an exchange, where the incoming star ejects the bound star and takes its place as a bound companion of the MBH (Section 4.4.2).

4.4.1. Tidal separation of a binary. The separation of a binary by the tidal field of an MBH is a mechanism that can accelerate stars to velocities $\gg v_{\star}$ (Hills 1988).¹⁸ Such HVSs can gain velocities well above the escape velocity from their galaxy of origin, thereby providing evidence for the existence of an MBH (or a binary MBH) in the galactic nucleus and providing information on the stellar population and the dynamics near the MBH and allowing us to probe the galactic potential.

4.4.1.1. Dynamics of tidal separation by an MBH. A binary of mass $M_{12} = M_1 + M_2$ and sma a_{12} that approaches the MBH on a parabolic orbit closer than $r_t = Q^{1/3} a_{12}$ (here $Q = M_{\bullet}/M_{12}$) is separated by the tidal field. The tidal work on the binary is $\Delta\epsilon_{12} \sim Q^{1/3} \epsilon_{12}$, where

¹⁸It is impossible to gravitationally accelerate a star to $\gg v_{\star}$ by non-destructive interaction with a perturbing mass, unless the perturber's own escape velocity is $\gg v_{\star}$, which implies an MBH (disruption cases 3 or 4; Section 4). This limits the possibilities to the interactions of a binary with a single MBH (Hills 1988), or of a single star with a binary MBH (Yu & Tremaine 2003).

$\epsilon_{12} = v_{12}^2 = GM_{12}/a_{12}$ is the relative velocity of the binary members. The radius of separation becomes the periape of the captured star (star 1), $r_{p1} = r_t = a_1(1 - e_1)$. The capture sma is $a_1 \sim GM_\star M_1/2M_{12}\Delta\epsilon_{12} \sim Q^{2/3}a_{12}/4$ (neglecting $\epsilon_{12} \ll \Delta\epsilon_{12}$ and for $M_1 = M_2$) and therefore $e_1 \sim 1 - Q^{-1/3} \sim 1$. The ejected star (star 2) acquires a velocity at infinity (neglecting the potential of the galaxy) $v_2 \sim \sqrt{2(M_{12}/M_2)\Delta\epsilon_{12}} \sim 2Q^{1/6}v_{12}$. For example, the capture of a $M_\star = 10M_\odot$, $R_\star = 4R_\odot$ S-star in the Galactic Center by the separation of an equal mass binary with $a_{12} = 1\text{ AU} \simeq 54R_\star$ would result an initial eccentricity $e_1 \simeq 0.98$ and sma $a_1 \simeq 0.004\text{ pc}$ ($P \simeq 12.5$ years). The ejection velocity would be $v_2 \simeq 2,000\text{ km s}^{-1}$, which is above the escape velocity from the Galaxy (Kenyon et al. 2008).

These order-of-magnitude estimates approximate a process that depends on many parameters (the internal orbital parameters of the binary and those of the binary’s center of mass relative to the MBH). A full statistical characterization of the outcomes requires three-body simulations (e.g., Kenyon et al. 2008, Zhang et al. 2010). However, because $Q \gg 1$, it is possible to apply a simpler approximate treatment (the restricted three-body problem), which reduces the number of parameters and yields some general results (Sari et al. 2010, Kobayashi et al. 2012): The ejection energy is not a strong function of the penetration depth (0.1–0.2 of binaries actually survive deep penetration); the more massive of the two stars carries a larger fraction of $\Delta\epsilon$, and so if $\epsilon > 0$ (unbound), the heavier member is preferentially ejected, whereas if $\epsilon < 0$, it is captured (in the limit $\epsilon \rightarrow 0$ the ejection/capture probabilities are independent of the stellar mass).

This simple picture of binary separation is further complicated by the finite size of the stars, which for some initial parameters results in stellar collisions and occasional mergers instead of ejections (Ginsburg & Loeb 2007; Antonini et al. 2010, 2011). A variation on the Hills mechanism consists of four-body interactions between an incoming triple system and the MBH, which ejects a hypervelocity short-period binary. A binary merger resulting in a rejuvenated star may explain some of the “too young” HVSs observed (Perets 2009).

Although the physics of the binary separation process are understood, quantitative predictions of the ejection rate and the HVS velocity distribution depend on poorly constrained properties of binaries in the Galactic Center (binary fraction, mass function, period distribution; Section 6.2) and on details of the loss-cone dynamics (Section 3).

4.4.1.2. Observed hypervelocity stars. At present, only HVSs ejected from the Milky Way are close enough to be detected. The first HVS was discovered by chance in a radial velocity survey of blue horizontal branch halo stars. HVS1, an $\sim 3M_\odot$ MS B-type star at a distance of $\sim 100\text{ kpc}$ and with velocity $> 673\text{ km s}^{-1}$ relative to the Galactic MBH, has at least twice the escape velocity from the Galaxy (Brown et al. 2005). Since that time, more than 20 unbound B-type stars were discovered in a systematic radial velocity survey [see detailed review by Brown (2015) for a summary of the current status of observations, observing strategies, other categories of detected HVSs, null results, and sample contamination by unrelated fast-moving stars]. Almost all the observed properties of the sample (metallicity, stellar rotation, stellar age and flight time, proper motion, bound/unbound ratio, number, and production rate) are either consistent with the Hills mechanism or not yet constraining enough. Two properties are in tension with theoretical predictions. The observed velocity distribution of HVSs does not extend to velocities as high as predicted (Rossi et al. 2014), which is a possible hint that the binary population is softer (has longer periods) than assumed. The spatial distribution of the HVS sample shows an anisotropy in Galactic longitude, which is not expected in the simplest Hills scenario. A sample of $\mathcal{O}(100)$ HVSs is required to discriminate between the different variants of MBH-assisted HVS ejections (Sesana et al. 2007).

The total HVS ejection rate (including all stellar types) that is derived from the observed sample, after correcting for sky coverage, HVS life spans, and the number fraction of B stars in the mass function, is $\sim 10^{-4} \text{ year}^{-1}$. This is close to the full loss-cone case assumed by Hills (1988), which can be justified if massive perturbers, likely GMCs, are efficiently scattering binaries into the loss cone (Perets et al. 2007; Section 2.1.3).

The trajectories of HVSSs, their velocity distribution, and the ratios between outgoing and infalling HVSSs all probe the Galactic potential, its symmetries, and the distribution of dark matter (Yu & Madau 2007, Kenyon et al. 2008, Perets et al. 2009b, Fragione & Loeb 2017, Rossi et al. 2016). The numbers of detected HVSSs are still not high enough for statistically robust conclusions, but this will improve with the upcoming GAIA astrometric data (Rossi et al. 2016).

4.4.1.3. Tidally captured stars. Tidal binary separation is a leading explanation for the S-star cluster observed in the central 1 arcsec $\simeq 0.04 \text{ pc}$ around Sgr A* (Gould & Quillen 2003). This would imply a direct correspondence between the S-stars and HVSSs, and indeed, the number and life span of the S-stars are consistent with the observed HVSSs (see above).

The near isothermal distribution of the S-star eccentricities, $n(e)de = 2ede$ (Gillessen et al. 2016), is consistent with neither the high capture eccentricity of tidal separation nor the low eccentricities that are expected if the S-stars migrated from the observed stellar disk (Sections 1.4 and 7). It is necessary to invoke postmigration dynamical evolution to explain the observations. *N*-body simulations indicate that fast SRR evolution in a steep cusp can reproduce the observed S-star eccentricities if they are tidally captured and in steady state. A dark cusp is necessary for generating strong enough RR torques. The disk origin scenario is disfavored (Perets et al. 2009a).

The fainter *B* stars on the 1-pc scale, which are on eccentric orbits and therefore probably not associated with the stellar disk, may have also been captured there by the Hills mechanism and should then be associated with slower, bound HVSSs (Madigan et al. 2014).

4.4.2. “Billiard balls” exchange. The masses of the S-stars around Sgr A* are $\mathcal{O}(10 M_{\odot})$, which is also the mass scale of stellar BHs that are believed to be strongly concentrated around Sgr A* due to mass segregation (Section 2.1.4). The similarity in mass scale suggests a possible connection, which may be realized dynamically by a three-body exchange interaction between an incoming B star on a radial orbit and a stellar BH on a tight orbit around the MBH. The exchange cross section is most effective when the exchanged stars have a similar mass (Heggie et al. 1996). Detailed calculations of the exchange cross section indicate that ~ 0.25 of the observed S-stars can be explained this way (Alexander & Livio 2004), with the limiting factors being the small exchange cross section and the number of B stars available for scattering toward the central arcsecond around Sgr A*. The continual replacement of mass-segregated stellar BHs by NS progenitors, and the analogous process of exchange of NSs by WD progenitors, may downsize the compact object population close to the MBH and play a role in regulating the buildup of the dark cusp.

5. RELATIVISTIC INTERACTIONS WITH AN MBH

The nature of the relativistic interactions accessible for stars near an MBH depends on r_t/R_{\bullet} , the tidal radius to event horizon ratio. ~ 1 - M_{\bullet} MS stars are disrupted outside R_{\bullet} for the $M_{\bullet} < 10^8 M_{\odot}$ MBHs considered here (Section 1.3.2). At $r \gtrsim r_t$, tidal interactions interfere with geodesic motion. It follows that only weak post-Newtonian effects are expected to be detectable in the orbits of MS stars (but see Freitag 2003). However, stellar BHs (and to a lesser extent NSs and WDs) can reach the event horizon unperturbed and therefore probe strong gravity.

5.1. Gravitational Waves from Extreme Mass–Ratio Inspirals

The emission of GWs from EMRIs provides clean tests of strong gravity. GR precession decouples the last stages of GW inspiral from the RR torques of the background stars (Section 3.2.3), and the nongeodetic drag by an accretion disk is negligible (Narayan 2000, Levin 2007). In addition, EMRIs can provide information about MBH demographics, stellar BHs, stellar dynamics in galactic nuclei, and cosmological parameters¹⁹ (see the review by Amaro-Seoane et al. 2007). The large mass ratio between the MBH and a stellar BH ($Q \gtrsim 10^5$) makes them test masses in the MBH’s space-time (once the BH’s small effect on space-time, its “self-force,” is taken into account; see the review by Barack 2009).

GWs are detected by measuring the relative change in distance, the strain $b = \Delta R/R$, due to the tidal effect of a time-varying metric. The lowest-order contribution to the time-dependent tidal far-field, $g' \sim \Delta g/R$, where g is the gravitational acceleration, comes from the fourth time derivative of the moment of inertia $I \sim M R^2$, $g' \sim G \ddot{I}/c^4 D$, where D is the distance to the MBH. The measured GW strain is therefore $b \sim \Delta R/R \sim \int dt (\int dt g') \sim G \ddot{I}/c^4 D \sim GM/c^4 R D$, where the time derivative is expressed by the typical angular frequency $\Omega^2 = GM/R^3$. For a BH, $R \sim r_g$, the strain is $b \sim r_g/D$ and the typical frequency is $f \sim 1/(2\pi t_g) = c^3/2\pi GM_\bullet$. For example, two grazing MBHs with total mass $10^7 M_\odot$ at a distance of 1 Gpc produce a strain of $b \sim \mathcal{O}(10^{-16})$ and $f \sim \mathcal{O}(10^{-3} \text{ Hz})$. For an EMRI ($M_\bullet \ll M_\star$), a detailed derivation yields (Thorne 1987)

$$b = \frac{\sqrt{2^7 \pi^{4/3}/15}}{Q} \frac{r_g}{D} (t_g f)^{2/3} \simeq 9 \times 10^{-23} \frac{M_\star}{10 M_\odot} \left(\frac{M_\bullet}{10^6 M_\odot} \frac{f}{10^{-3} \text{ Hz}} \right)^{2/3} \left(\frac{D}{1 \text{ Gpc}} \right)^{-1}. \quad (8)$$

Planned low-frequency (millihertz) spaceborne GW detectors (eLISA Consortium 2016), which are optimal for the $M_\bullet \sim \mathcal{O}(10^6 M_\odot)$ mass scale, will observe the entire sky. An EMRI spends a few years, and goes through $>10^5$ cycles, while in the detection band. A simple estimate of the number of expected GW sources, assuming an EMRI rate of $\Gamma_i = 10^{-6} \text{ year}^{-1} \text{ gal}^{-1}$ (Figure 6) for $N = 10^8$ Milky Way–like galaxies inside $z = 1$ over a 1-year mission, suggests $\mathcal{O}(100)$ EMRIs simultaneously emitting in the detection band. Because of the tiny strain and possible source confusion, detection of GWs from distant galaxies must rely on precalculated waveform templates and on the statistics provided by the large number of quasi-periodic GW cycles. The templates depend on the eccentricity of the final orbits, which reflect the dynamics leading to the inspiral. GW dissipation of energy and angular momentum generally drives EMRI orbits to circularization. However, EMRIs that began on eccentric loss-cone orbits tend to retain a fairly high eccentricity (Hopman & Alexander 2005); EMRIs captured by binary tidal separation will be circular (Miller et al. 2005); EMRIs captured or formed in the disk will be circular and in the equatorial plane of the MBH (Section 7.1).

5.2. Stars and Pulsars on Relativistic Orbits in the Galactic Center

Post-Newtonian phenomena that may be observed around Sgr A* include the lowest-order effects of gravitational redshift and relativistic Doppler shift, which are already detectable near periapease passage with available spectroscopy (Zucker et al. 2006). Relativistic precession of stars on very

¹⁹The measurables from an EMRI are $M_\star(1+z)$, χ_\bullet (MBH dimensionless spin parameter); $M_\star(1+z)$, e , i (inclination angle); D_L (luminosity distance); and sky position (Barack & Cutler 2004). A redshift determination from an electromagnetic counterpart, if available, breaks the redshift/mass degeneracy and constrains a combination of the cosmological parameters H_0 , Ω_M , and Ω_Λ .

short-period orbits could be detected by the adaptive optics–assisted IR interferometer GRAVITY (Eisenhauer et al. 2011) and test the “no-hair” theorem (Will 2008). RR perturbations by background stars are a major concern, with the exception of polar orbits relative to the MBH spin axis χ_* (Merritt et al. 2010), where the out-of plane Lense–Thirring precession and quadrupole precession provide AI protection against the stellar perturbations (Section 3.2.2). It is not clear how many stars exist on very relativistic orbits, given the short survival time so close to the MBH. High-precision measurement of radio pulsars could accurately map space-time around the MBH (see the review by Eatough et al. 2015). It may be possible to circumvent the stellar perturbations by using data only from the fraction of the orbit near periaapse, where the perturbations are small (Psaltis et al. 2016). However, it should be noted that only one pulsar (a magnetar; Kennea et al. 2013) has been found to date near Sgr A*. It is not clear whether this is due to strong electron scattering along some lines of sight or whether, contrary to expectations, radio-emitting NSs are inherently rare in that environment. Finally, it is possible that EMRIs from very low-mass stars, which are dense enough to withstand the MBH tides, will be detected (Freitag 2003) and that gravitational lensing of background stars by the MBH and stellar BHs around it will be observed (Wardle & Yusef-Zadeh 1992, Alexander & Sternberg 1999, Alexander & Loeb 2001, Alexander 2001, Nusser & Broadhurst 2004).

6. STAR-STAR COLLISIONS NEAR AN MBH

The rate of physical star–star collisions, per star, is $\Gamma_c \simeq 16\sqrt{\pi}n_*\sigma R_*^2[1 + (v_*/\sigma)^2]$, where the term $(v_*/\sigma)^2$ expresses the effect of gravitational focusing, and a Maxwellian velocity distribution with dispersion $\sigma^2 \sim GM_*/r$ is assumed (e.g., Binney & Tremaine 2008). Close enough to the MBH, where $\sigma > v_*$, inside the collision radius $r_{\text{coll}} = QR_* = (c/v_*)^2 r_g \sim \mathcal{O}(10^5)r_g$ (Section 1.3.4), the collision rate rapidly increases as $\Gamma_c \propto r^{-\alpha-1/2}$ (in an $n_* \propto r^{-\alpha}$ cusp) until the mean time between collisions becomes shorter than the stellar life span, and the system is dominated by physical collisions. Because the kinetic energy in the colliding star exceeds the binding energy, the collisions lead to stellar destruction rather than to mergers, whether in a single head-on collision or in several grazing collisions that lead to mass loss. Such high-velocity collisions are unique to the near environment of an MBH.

6.1. Collisional Destruction and Mergers

The outcome of fast star–star encounters depends on the impact parameter, the escape velocity from the surface of the stars, and the stellar structure. Three types of such encounters are briefly discussed here.

6.1.1. Collisional stripping of red giant envelopes. The absence of the brightest red giants ($K < 13.5^m$) in the central ~ 1 arcsec (~ 0.04 pc) of the Galactic Center has led to suggestions that this may be the result of collisional envelope stripping. The envelope’s dynamical and thermal timescales are short; a hole “punched out” by a star passing through it would be quickly filled. Lasting damage to the giant can only be achieved if the impactor kicks the giant’s core out of the envelope or forms a common-envelope binary (Livne & Tuchman 1988). This requires a nearly head-on collision for the high velocities near Sgr A* or a collision with a binary (Bailey & Davies 1999). Giant envelope stripping by collisions with single stars and binaries is consistent with the observations in the central 1 arcsec, if a high-density power-law cusp is assumed (Alexander 1999). However, it cannot explain the depletion of the higher-luminosity giants ($K < 12^m$) farther out

on the 5-arcsec scale. To do that would require a large population of stellar BHs (Dale et al. 2009), which is inconsistent with the drain limit (Section 2.1.4) or with the dynamical mass measurements in the Galactic Center.

6.1.2. Tidal spin-up. Nondestructive close stellar collisions excite tides on the two stars, which lead to energy dissipation, tidal torquing, and possible mass loss. The random orbital orientations of successive close encounters over the lifetimes of long-lived low-mass stars can build up a substantial stellar spin by random walk (assuming inefficient magnetic breaking). Over time the low-mass stars around the MBH are expected to spin at 0.1–0.3 of the centrifugal breakup velocity (Alexander & Kumar 2001). Such high rotation may explain the strong coronal radiation that is observed around Sgr A* (Sazonov et al. 2012).

6.1.3. Collisional destructions/mergers. The region depleted of red giants in the Galactic Center happens to overlap with the region where many young blue stars are observed. This coincidence motivates the search for a “rejuvenation” mechanism (Ghez et al. 2003) that can transform an old red giant into a young-looking stellar object (Section 7.1). Stellar collisions and mergers were discussed in this context. However, hydrodynamical simulations overall confirm the simple physical analysis presented above: Fast off-center collisions are inefficient in substantially changing the star (although many repeated collisions may whittle it gradually down; Rauch 1999), whereas fast head-on collisions are disruptive (Lai et al. 1993, Freitag & Benz 2005). Although some exotic merger products may exist around Sgr A*, it is unlikely mergers can explain a substantial fraction of the population.

6.2. Collisions Involving Binaries

Binaries near an MBH are not as dynamically important as binaries in clusters, where they control the evolution (e.g., Binney & Tremaine 2008), because the single stars are tightly bound to the MBH. However, they may play other roles, for example, in HVS ejection and tidal captures; tidally captured stars can become EMRIs or be tidally disrupted; binaries can acquire a compact companion by evolution or exchange and appear as X-ray sources or produce millisecond pulsars that can be used to probe space-time around the MBH (Section 5.2); binary mergers may produce massive blue stars that are observed in the Galactic Center, whose origin is uncertain.

The fraction of binaries among the stars inside r_h is not well known. The small number of massive young binaries detected in the Galactic Center is consistent with the binary fraction in young stellar clusters elsewhere in the Galaxy (Pfuhl et al. 2014). The overabundance of transient X-ray sources in the inner 1 pc of the Galactic Center, identified as NS/BH low- or high-mass X-ray binaries (Muno et al. 2005), likewise hints that binaries, or at least high-mass binaries, do exist inside r_h .

Long-lived low-mass binaries are gradually evaporated by three-body interactions with single stars in a high-density stellar cusp, and their fraction drops with proximity to the MBH (Hopman 2009a). Conversely, the existence of low-mass binaries near Sgr A*, if such are detected, will place an upper bound on the local stellar density (and a lower bound on the local NR time) and thereby reveal a dark cusp around the MBH (Alexander & Pfuhl 2014).

Internal collisions and mergers between the binary components can be induced by Kozai–Lidov oscillations due to the MBH (acting as an external perturber in the binary’s frame; see the review by Naoz 2016) (Antonini et al. 2010, Prodan et al. 2015, Stephan et al. 2016) and also in the course of a binary separation event (Section 4.4.1).

7. STARS AND CIRCUMNUCLEAR ACCRETION DISKS

A circumnuclear accretion disk is embedded in a dense circumnuclear cluster. It is plausible that the two are strongly coupled. Many studies have explored a wide range of possible mechanisms and implications. These are categorized here in several broad themes.

7.1. Hydrodynamical Star-Disk Interactions

One way stars can interact with an accretion disk is by crossing through it or by orbiting inside it. The hydrodynamical interaction due to the passage of a dense body through the disk gas can affect the accretion flow and change the star's mass and orbit.

7.1.1. Stellar trapping, growth, and destruction. Stars whose eccentric orbits intersect the disk experience drag and gradually settle into circular corotating orbits (Ostriker 1983, Syer et al. 1991). Once embedded in the disk, they migrate inward, in some cases opening a gap in the disk and in others continuously growing by accreting mass from it. The star perturbs the disk and can excite periodic AGN variability. If the stellar accretion and evolutionary timescales are faster than the migration, the stars will explode as SNe while in the disk, thereby raising its metallicity early on, as is observed in high- z quasars (Artymowicz et al. 1993). Stars that open a gap in the disk and migrate to its inner edge before exploding will interrupt the gas supply and cause a transient dimming and reddening of the quasar (Goodman & Tan 2004) and ultimately be tidally disrupted. Remnants trapped in the disk or formed following disk growth and SNe explosions can reach short-period relativistic orbits and become EMRI GW sources (Levin 2007).

A major puzzle is the suppression of red giants in the inner ~ 0.5 pc of the Galactic Center, contrary to theoretical expectations of a high-density cusp (Section 1.4). Intriguingly, this length scale coincides with the extent of the ~ 6 -Myr-old stellar disk, which is believed to have formed from a gravitationally unstable gas disk. Interactions between such a clumpy gas disk and red giants that cross it can gradually strip the giants of their envelopes even over the short time the disk exists at this marginally stable phase, provided that the giants expand in response to partial stripping (Amaro-Seoane & Chen 2014). Hydrodynamical simulations provide some support for this scenario (Kieffer & Bogdanović 2016). Such selective stripping, if true, implies that the giants do not trace the faint population.

7.1.2. Stars and mass accretion rate. Accretion requires a mechanism to transport angular momentum outward through the disk to some sink. Stars can play various roles in the disk's angular momentum transfer. The gravitational drag on stars crossing the disk extracts angular momentum from the disk on the NR timescale (Ostriker 1983). This is too slow compared to the viscous rate typically assumed for AGN disks, unless the MBH is very low mass (IMBH scale) or the disk is very thin (cold). SNe in the disk can redistribute angular momentum at a rate equivalent to that assumed for a typical AGN accretion disk (Rozyczka et al. 1995). In analogy to migration in protoplanetary disks, a single massive star undergoing type III (outward) migration in an AGN disk can extract enough angular momentum to generate AGN accretion rates (McKernan et al. 2011).

The accretion rate may be regulated by the rate $\Gamma_i(\sigma)$ (Equation 6) at which stars are scattered to eccentric disk-crossing orbits and eventually get trapped in it. This connects σ and M_\bullet and may explain the M_\bullet/σ relation (Miralda-Escudé & Kollmeier 2005).

7.2. Gravitational Star–Disk Interactions (Disk Warping)

A thin accretion disk, whose radial inflow velocity is much slower than the near-Keplerian circular velocity, can be viewed as a set of concentric mass rings that are coupled by their internal viscous stresses. VRR exerts torques on the disk (Section 2.2) with spatial coherence scale $\Delta \log a \sim 1$ (Section 2.2) and temporal coherence timescale T_c^{SQ} . The VRR torques warp the disk [assumed to extend over $\log(a_{\text{max}}/a_{\text{min}}) \gg 1$] but are countered by the disk’s out-of-plane viscous torques that flatten it. Scaling arguments and simulations (Bregman & Alexander 2009, 2012) show that the gravitational RR torques are stronger than the hydrodynamical drag torques by stars crossing the disk (Section 7.1) for $M_\bullet \gtrsim \text{few} \times 10^4 M_\odot$ and that the external RR torques are stronger than the internal viscous torques for $M_\bullet < \mathcal{O}(10^7 M_\odot)$. Therefore disks around lighter MBHs warp under the influence of VRR, whereas disks around more massive MBHs rotate as solid bodies.

Warping by RR affects the physical properties and dynamics of the disk (Bregman & Alexander 2012). The warps expose the disk to the ionizing continuum from the central source, thereby increasing its viscosity and modifying its line emission. The continual warping of the disk extracts angular momentum and thereby increases the mass accretion rate (Lodato & Pringle 2006). The Bardeen–Petterson frame-dragging effect couples the stellar torques to the MBH spin via the warps. This leads to a jitter in the spin direction, which may translate to a jitter in the radio jet direction if it is aligned with MBH spin axis.

This RR-driven disk warping scenario can be tested by modeling observed warps in maser disks. Circumnuclear maser disks are typically found around MBHs with $M_\bullet \sim 10^7 M_\odot$ and display warps of a few degrees (Kuo et al. 2011). In particular, the well-studied maser disk in AGN NGC 4258 shows an 8° warp (Miyoshi et al. 1995), which is consistently and naturally reproduced (in the statistical sense) by stellar RR torques (Bregman & Alexander 2012).

7.3. Disk Fragmentation and Star Formation

The young stellar disk around Sgr A* (Bartko et al. 2009, Lu et al. 2009) provides compelling indications that star formation can occur in situ in a circumnuclear disk. This unusual formation mode is quite unlike that observed in the galactic field, where stars form in dense, cold self-gravitating molecular clouds. The observed stellar disk is naturally explained by the gravitational instability and fragmentation of a gas disk, similar to observed circumnuclear maser disks (Milosavljević & Loeb 2004). The initial stellar mass function in a fragmenting disk is likely top-heavy (Levin 2007). Low-mass ($\lesssim 3 M_\odot$) young stellar objects produce copious X-rays, which are not observed. This is consistent with a top-heavy initial mass function with an $\sim 3 M_\odot$ lower-mass cutoff (Nayakshin & Sunyaev 2005).

8. FUTURE PROSPECTS

Over the next two decades, major new instruments are expected to provide tools and opportunities for studying galactic nuclei, MBHs, and strong gravity. Already operating are the VLT/GRAVITY interferometer (Eisenhauer et al. 2011), which is looking for low-mass stars on relativistic orbits around Sgr A* with unprecedented astrometric precision, and large-scale transient source surveys (Pan-STARRS, Kaiser et al. 2002; PTF/ZTF, Law et al. 2009, Bellm 2014; ASAS-SN, Shappee et al. 2014), which search for TDEs.

Pulsars on relativistic orbits around Sgr A* may be detected in a few years with the next-generation millimeter observatories (LMT, phased-NOEMA, phased-ALMA) and by the radio Square Kilometer Array (Eatough et al. 2015). In a decade, extremely large telescopes (E-ELT,

TMT) will dramatically improve the ability to observe fine details in galactic nuclei. In two decades, the low-frequency spaceborne GW detector eLISA will detect EMRIs to $z \lesssim 0.5$ and essentially all MBH–MBH mergers (eLISA Consortium 2016).

The prospects of precision GR tests with GWs, MBH astronomy with GWs and TDEs, and detailed observations of the Galactic Center and of external galactic nuclei with extremely large telescopes are continuing to motivate deeper understanding and high-fidelity modeling of these processes across all the relevant theoretical subfields.

DISCLOSURE STATEMENT

The author is not aware of any affiliations, memberships, funding, or financial holdings that might be perceived as affecting the objectivity of this review.

ACKNOWLEDGMENTS

I am grateful for helpful comments by Ben Bar-Or and Elena Rossi. This work was supported by the I-CORE Program of the PBC and the ISF (grant number 1829/12).

LITERATURE CITED

- Alexander T. 1999. *Ap. J.* 527:835–50
- Alexander T. 2001. *Ap. J. Lett.* 553:L149–52
- Alexander T. 2005. *Phys. Rep.* 419:65–142
- Alexander T. 2010. In *Astro-GR@Paris 2010: Gravitational-Wave and Electromagnetic Signatures of Massive Black Hole Binaries and Extreme Mass-Ratio Inspirals*, APC, Paris, Sept. 13–17. <http://astro-gr.org/astro-gr-2010-gw-em-signatures-massive-black-hole-binaries-emris/>
- Alexander T. 2011. In *The Galactic Center: a Window to the Nuclear Environment of Disk Galaxies*, ed. MR Morris, QD Wang, F Yuan. *ASP Conf. Ser.* 439:129. San Francisco: ASP
- Alexander T. 2012. In *Tidal Disruption and AGN Outburst*. *Eur. Phys. J. Web Conf.* 39:05001
- Alexander T. 2015. In *Proc. 50th Recontres Moriond Gravit.: 100 Years After GR, La Thuile, Italy, March 21–28*. arXiv:1505.04823
- Alexander T, Hopman C. 2003. *Ap. J. Lett.* 590:L29–32
- Alexander T, Hopman C. 2009. *Ap. J.* 697:1861–69
- Alexander T, Kumar P. 2001. *Ap. J.* 549:948–58
- Alexander T, Livio M. 2001. *Ap. J. Lett.* 560:L143–46
- Alexander T, Livio M. 2004. *Ap. J. Lett.* 606:L21–24
- Alexander T, Loeb A. 2001. *Ap. J.* 551:223–30
- Alexander T, Morris M. 2003. *Ap. J. Lett.* 590:L25–28
- Alexander T, Natarajan P. 2014. *Science* 345:1330–33
- Alexander T, Pfuhl O. 2014. *Ap. J.* 780:148
- Alexander T, Sternberg A. 1999. *Ap. J.* 520:137–48
- Amaro-Seoane P, Chen X. 2014. *Ap. J. Lett.* 781:L18
- Amaro-Seoane P, Gair JR, Freitag M, et al. 2007. *Class. Quantum Gravity* 24:113
- Antonini F. 2014. *Ap. J.* 794:106
- Antonini F, Faber J, Gualandris A, Merritt D. 2010. *Ap. J.* 713:90–104
- Antonini F, Lombardi JC Jr., Merritt D. 2011. *Ap. J.* 731:128
- Antonini F, Merritt D. 2013. *Ap. J. Lett.* 763:L10
- Arcavi I, Gal-Yam A, Sullivan M, et al. 2014. *Ap. J.* 793:38
- Artymowicz P, Lin DNC, Wampler EJ. 1993. *Ap. J.* 409:592–603
- Bahcall JN, Wolf RA. 1977. *Ap. J.* 216:883–907
- Bailey VC, Davies MB. 1999. *MNRAS* 308:257–70
- Bar-Or B, Alexander T. 2014. *Class. Quantum Gravity* 31:244003

- Bar-Or B, Alexander T. 2016. *Ap. J.* 820:129
- Bar-Or B, Kupi G, Alexander T. 2013. *Ap. J.* 764:52
- Barack L. 2009. *Class. Quantum Gravity* 26:213001
- Barack L, Cutler C. 2004. *Phys. Rev. D* 69:082005
- Bardeen JM, Petterson JA. 1975. *Ap. J. Lett.* 195:L65
- Bartko H, Martins F, Fritz TK, et al. 2009. *Ap. J.* 697:1741–63
- Bartko H, Martins F, Tripp S, et al. 2010. *Ap. J.* 708:834–40
- Begelman MC, Blandford RD, Rees MJ. 1980. *Nature* 287:307–9
- Bellm E. 2014. In *Proc. 3rd Hot-Wiring Transient Universe Workshop*, ed. PR Wozniak, MJ Graham, AA Mahabal, R Seaman, pp. 27–33. Los Alamos, NM: Los Alamos Natl. Lab.
- Binney J, Tremaine S. 2008. *Galactic Dynamics*. Princeton, NJ: Princeton Univ. Press. 2nd ed.
- Boehle A, Ghez AM, Schödel R, et al. 2016. *Ap. J.* 830:17
- Bonnerot C, Rossi EM, Lodato G. 2016. *MNRAS* 458:3324–30
- Bonnerot C, Rossi EM, Lodato G, Price DJ. 2016. *MNRAS* 455:2253–66
- Bregman M, Alexander T. 2009. *Ap. J. Lett.* 700:L192–95
- Bregman M, Alexander T. 2012. *Ap. J.* 748:63
- Brem P, Amaro-Seoane P, Sopuerta CF. 2014. *MNRAS* 437:1259–67
- Brown WR. 2015. *Annu. Rev. Astron. Astrophys.* 53:15–49
- Brown WR, Geller MJ, Kenyon SJ, Kurtz MJ. 2005. *Ap. J. Lett.* 622:L33–36
- Buchholz RM, Schödel R, Eckart A. 2009. *Astron. Astrophys.* 499:483–501
- Callen HB, Welton TA. 1951. *Phys. Rev.* 83:34–40
- Carr JS, Sellgren K, Balachandran SC. 2000. *Ap. J.* 530:307–22
- Carter B, Luminet JP. 1982. *Nature* 296:211–14
- Chatterjee P, Hernquist L, Loeb A. 2002. *Phys. Rev. Lett.* 88:121103
- Chen X, Sesana A, Madau P, Liu FK. 2011. *Ap. J.* 729:13
- Dai L, Escala A, Coppi P. 2013. *Ap. J. Lett.* 775:L9
- Dai L, McKinney JC, Miller MC. 2015. *Ap. J. Lett.* 812:L39
- Dale JE, Davies MB, Church RP, Freitag M. 2009. *MNRAS* 393:1016–33
- Davies MB, Miller MC, Bellovary JM. 2011. *Ap. J. Lett.* 740:L42
- Dearborn DSP, Wilson JR, Mathews GJ. 2005. *Ap. J.* 630:309–20
- Deegan P, Nayakshin S. 2007. *MNRAS* 377:897–904
- Devecchi B, Volonteri M. 2009. *Ap. J.* 694:302–13
- Do T, Ghez AM, Morris MR, et al. 2009. *Ap. J.* 703:1323–37
- Eatough R, Lazio TJW, Casanellas J, et al. 2015. In *Adv. Astrophys. Sq. Kilometre Array, Giardini Naxos, Italy, Jun. 8–13. Proc. Sci. (AASKA14):045*
- Eilon E, Kupi G, Alexander T. 2009. *Ap. J.* 698:641–47
- Eisenhauer F, Perrin G, Brandner W, et al. 2011. *Messenger* 143:16–24
- eLISA Consortium. 2016. *The gravitational universe*. arXiv:1305.5720
- Ferrarese L, Merritt D. 2000. *Ap. J. Lett.* 539:L9–12
- Fouvry JB, Pichon C, Magorrian J. 2016. *Astron. Astrophys.* In press. arXiv:1606.05501
- Fragione G, Loeb A. 2017. *New Astron.* 55:32–38
- Frank J, Rees MJ. 1976. *MNRAS* 176:633–47
- Freitag M. 2003. *Ap. J. Lett.* 583:L21–24
- Freitag M, Benz W. 2002. *Astron. Astrophys.* 394:345–74
- Freitag M, Benz W. 2005. *MNRAS* 358:1133–58
- French KD, Arcavi I, Zabludoff A. 2016. *Ap. J. Lett.* 818:L21
- Fritz TK, Chatzopoulos S, Gerhard O, et al. 2016. *Ap. J.* 821:44
- Gebhardt K, Bender R, Bower G, et al. 2000. *Ap. J. Lett.* 539:L13–L16
- Genzel R, Eisenhauer F, Gillessen S. 2010. *Rev. Mod. Phys.* 82:3121–95
- Genzel R, Pichon C, Eckart A, Gerhard OE, Ott T. 2000. *MNRAS* 317:348–74
- Georgiev IY, Böker T, Leigh N, Lützgendorf N, Neumayer N. 2016. *MNRAS* 457:2122–38
- Gerhard OE, Binney J. 1985. *MNRAS* 216:467–502
- Ghez AM, Duchêne G, Matthews K, et al. 2003. *Ap. J. Lett.* 586:L127–31

- Gillessen S, Eisenhauer F, Trippe S, et al. 2009. *Ap. J.* 692:1075–109
- Gillessen S, Genzel R, Fritz TK, et al. 2012. *Nature* 481:51–54
- Gillessen S, Plewa P, Eisenhauer F, et al. 2016. *Ap. J.* 837(1):30
- Ginsburg I, Loeb A. 2007. *MNRAS* 376:492–96
- Goodman J. 1983. *Ap. J.* 270:700
- Goodman J, Tan JC. 2004. *Ap. J.* 608:108–18
- Gould A, Quillen AC. 2003. *Ap. J.* 592:935–40
- Graham AW. 2016. In *Galactic Bulges*, ed. E Laurikainen, R Peletier, D Gadotti. *Astrophys. Space Sci. Libr.* 418:263–313. Cham, Switz.: Springer Int. Publ.
- Guillochon J, Loeb A, MacLeod M, Ramirez-Ruiz E. 2014. *Ap. J. Lett.* 786:L12
- Guillochon J, Ramirez-Ruiz E. 2013. *Ap. J.* 767:25
- Guillochon J, Ramirez-Ruiz E. 2015. *Ap. J.* 809:166
- Gürkan MA, Hopman C. 2007. *MNRAS* 379:1083–88
- Häring N, Rix HW. 2004. *Ap. J. Lett.* 604:L89–92
- Hayasaki K, Stone N, Loeb A. 2016. *MNRAS* 461:3760–80
- Heggie D, Hut P. 2003. *The Gravitational Million-Body Problem: A Multidisciplinary Approach to Star Cluster Dynamics*. Cambridge, UK: Cambridge Univ. Press. 372 pp.
- Heggie DC, Hut P, McMillan SLW. 1996. *Ap. J.* 467:359
- Hills JG. 1988. *Nature* 331:687–89
- Hopman C. 2009a. *Ap. J.* 700:1933–51
- Hopman C. 2009b. *Class. Quantum Gravity* 26:094028
- Hopman C, Alexander T. 2005. *Ap. J.* 629:362–72
- Hopman C, Alexander T. 2006. *Ap. J.* 645:1152–63
- Kaiser N, Aussel H, Burke BE, et al. 2002. In *Survey and Other Telescope Technologies and Discoveries*, ed. JA Tyson, S Wolff. *Proc. SPIE Conf. Ser.* 4836:154. Bellingham, WA: SPIE
- Kauffmann G, Heckman TM, Tremonti C, et al. 2003. *MNRAS* 346:1055–77
- Kennea JA, Burrows DN, Kouveliotou C, et al. 2013. *Ap. J. Lett.* 770:L24
- Kenyon SJ, Bromley BC, Geller MJ, Brown WR. 2008. *Ap. J.* 680:312–27
- Keshet U, Hopman C, Alexander T. 2009. *Ap. J. Lett.* 698:L64–67
- Kieffer TF, Bogdanović T. 2016. *Ap. J.* 823:155
- King A, Pounds K. 2015. *Annu. Rev. Astron. Astrophys.* 53:115–54
- Kobayashi S, Hainick Y, Sari R, Rossi EM. 2012. *Ap. J.* 748:105
- Kocsis B, Tremaine S. 2015. *MNRAS* 448:3265–96
- Komossa S. 2015. *J. High Energy Astrophys.* 7:148–57
- Kormendy J, Bender R. 2009. *Ap. J. Lett.* 691:L142–46
- Kormendy J, Ho LC. 2013. *Annu. Rev. Astron. Astrophys.* 51:511–653
- Kuo CY, Braatz JA, Condon JJ, et al. 2011. *Ap. J.* 727:20
- Laguna P, Miller WA, Zurek WH, Davies MB. 1993. *Ap. J. Lett.* 410:L83–86
- Lai D, Rasio FA, Shapiro SL. 1993. *Ap. J.* 412:593–611
- Lasota JP, Alexander T, Dubus G, et al. 2011. *Ap. J.* 735:89
- Lauer TR, Faber SM, Ajhar EA, Grillmair CJ, Scowen PA. 1998. *Astron. J.* 116:2263–86
- Law NM, Kulkarni SR, Dekany RG, et al. 2009. *Publ. Astron. Soc. Pac.* 121:1395–408
- Levin Y. 2007. *MNRAS* 374:515–24
- Levin Y, Beloborodov AM. 2003. *Ap. J. Lett.* 590:L33–36
- Li YR, Ho LC, Wang JM. 2011. *Ap. J.* 742:33
- Lightman AP, Shapiro SL. 1977. *Ap. J.* 211:244–62
- Livne E, Tuchman Y. 1988. *Ap. J.* 332:271–81
- Lodato G, King AR, Pringle JE. 2009. *MNRAS* 392:332–40
- Lodato G, Pringle JE. 2006. *MNRAS* 368:1196–208
- Lu JR, Do T, Ghez AM, et al. 2013. *Ap. J.* 764:155
- Lu JR, Ghez AM, Hornstein SD, et al. 2009. *Ap. J.* 690:1463–87
- Luminet JP, Pichon B. 1989. *Astron. Astrophys.* 209:103–10
- MacLeod M, Guillochon J, Ramirez-Ruiz E. 2012. *Ap. J.* 757:134

- Madigan AM, Hopman C, Levin Y. 2011. *Ap. J.* 738:99
- Madigan AM, Pfuhl O, Levin Y, et al. 2014. *Ap. J.* 784:23
- Maeda Y, Baganoff FK, Feigelson ED, et al. 2002. *Ap. J.* 570:671–87
- Magorrian J, Tremaine S. 1999. *MNRAS* 309:447–60
- Magorrian J, Tremaine S, Richstone D, et al. 1998. *Astron. J.* 115:2285–305
- Maness H, Martins F, Trippe S, et al. 2007. *Ap. J.* 669:1024–41
- Manukian H, Guillochon J, Ramirez-Ruiz E, O’Leary RM. 2013. *Ap. J. Lett.* 771:L28
- McConnell NJ, Ma CP, Gebhardt K, et al. 2011. *Nature* 480:215–18
- McKernan B, Ford KES, Lyra W, et al. 2011. *MNRAS* 417:L103–7
- Merritt D. 2010. *Ap. J.* 718:739–61
- Merritt D. 2013. *Dynamics and Evolution of Galactic Nuclei*. Princeton, NJ: Princeton Univ. Press
- Merritt D, Alexander T, Mikkola S, Will CM. 2010. *Phys. Rev. D* 81:062002
- Merritt D, Alexander T, Mikkola S, Will CM. 2011. *Phys. Rev. D* 84:044024
- Merritt D, Berczik P, Laun F. 2007. *Astron. J.* 133:553–63
- Merritt D, Milosavljević M. 2005. *Living Rev. Relativ.* 8:8
- Mikkola S, Merritt D. 2006. *MNRAS* 372:219–23
- Miller MC, Colbert EJM. 2004. *Int. J. Mod. Phys. D* 13:1–64
- Miller MC, Freitag M, Hamilton DP, Lauburg VM. 2005. *Ap. J. Lett.* 631:L117–20
- Milosavljević M, Loeb A. 2004. *Ap. J. Lett.* 604:L45–48
- Milosavljević M, Merritt D. 2001. *Ap. J.* 563:34–62
- Milosavljević M, Merritt D, Rest A, van den Bosch FC. 2002. *MNRAS* 331:L51–55
- Miralda-Escudé J, Kollmeier JA. 2005. *Ap. J.* 619:30–40
- Miyoshi M, Moran J, Herrnstein J, et al. 1995. *Nature* 373:127–29
- Mo H, van den Bosch F, White S. 2010. *Galaxy Formation and Evolution*. Cambridge, UK: Cambridge Univ. Press
- Morris M. 1993. *Ap. J.* 408:496–506
- Mortlock DJ, Warren SJ, Venemans BP, et al. 2011. *Nature* 474:616–19
- Muno MP, Pfahl E, Baganoff FK, et al. 2005. *Ap. J. Lett.* 622:L113–16
- Murphy BW, Cohn HN, Durisen RH. 1991. *Ap. J.* 370:60–77
- Naoz S. 2016. *Annu. Rev. Astron. Astrophys.* 54:441–89
- Narayan R. 2000. *Ap. J.* 536:663–67
- Nayakshin S, Sunyaev R. 2005. *MNRAS* 364:L23–27
- Netzer H. 2015. *Annu. Rev. Astron. Astrophys.* 53:365–408
- Novikov ID, Pethick CJ, Polnarev AG. 1992. *MNRAS* 255:276–84
- Nusser A, Broadhurst T. 2004. *MNRAS* 355:L6–8
- Omukai K, Schneider R, Haiman Z. 2008. *Ap. J.* 686:801–14
- Ostriker JP. 1983. *Ap. J.* 273:99–104
- Perets HB. 2009. *Ap. J.* 698:1330–40
- Perets HB, Gualandris A, Kupi G, Merritt D, Alexander T. 2009a. *Ap. J.* 702:884–89
- Perets HB, Hopman C, Alexander T. 2007. *Ap. J.* 656:709–20
- Perets HB, Wu X, Zhao HS, et al. 2009b. *Ap. J.* 697:2096–101
- Pfuhl O, Alexander T, Gillessen S, et al. 2014. *Ap. J.* 782:101
- Phifer K, Do T, Meyer L, et al. 2013. *Ap. J. Lett.* 773:L13
- Press WH, Teukolsky SA. 1977. *Ap. J.* 213:183–92
- Preto M, Amaro-Seoane P. 2010. *Ap. J. Lett.* 708:L42–46
- Prodan S, Antonini F, Perets HB. 2015. *Ap. J.* 799:118
- Psaltis D, Wex N, Kramer M. 2016. *Ap. J.* 818:121
- Rauch KP. 1999. *Ap. J.* 514:725–45
- Rauch KP, Tremaine S. 1996. *New Astron.* 1:149–70
- Rees MJ. 1988. *Nature* 333:523–28
- Rossi EM, Kobayashi S, Sari R. 2014. *Ap. J.* 795:125
- Rossi EM, Marchetti T, Cacciato M, Kuiack M, Sari R. 2016. *MNRAS* 467(2):1844–56
- Rosswog S, Ramirez-Ruiz E, Hix WR. 2009. *Ap. J.* 695:404–19

- Rozyczka M, Bodenheimer P, Lin DNC. 1995. *MNRAS* 276:597–606
- Sari R, Kobayashi S, Rossi EM. 2010. *Ap. J.* 708:605–14
- Sazonov S, Sunyaev R, Revnivtsev M. 2012. *MNRAS* 420:388–404
- Schaller G, Schaerer D, Meynet G, Maeder A. 1992. *Astron. Astrophys. Suppl.* 96:269–331
- Schödel R, Eckart A, Alexander T, et al. 2007. *Astron. Astrophys.* 469:125–46
- Schödel R, Gallego Cano E, Dong H, et al. 2016. Presented at 11th LISA Symp., Zurich, Switz.
- Sesana A, Haardt F, Madau P. 2007. *MNRAS* 379:L45–49
- Shapiro SL, Marchant AB. 1978. *Ap. J.* 225:603–24
- Shappee BJ, Prieto JL, Grupe D, et al. 2014. *Ap. J.* 788:48
- Soltan A. 1982. *MNRAS* 200:115–22
- Spitzer LJ. 1969. *Ap. J. Lett.* 158:L139–42
- Spitzer LJ, Schwarzschild M. 1951. *Ap. J.* 114:385–97
- Stephan AP, Naoz S, Ghez AM, et al. 2016. *MNRAS* 460:3494–504
- Stone N, Sari R, Loeb A. 2013. *MNRAS* 435:1809–24
- Stone NC, Metzger BD. 2016. *MNRAS* 455:859–83
- Stone NC, van Velzen S. 2016. *Ap. J. Lett.* 825:L14
- Syer D, Clarke CJ, Rees MJ. 1991. *MNRAS* 250:505–12
- Syer D, Ulmer A. 1999. *MNRAS* 306:35–42
- Thomas J, Saglia RP, Bender R, Erwin P, Fabricius M. 2014. *Ap. J.* 782:39
- Thorne KS. 1987. In *Three Hundred Years of Gravitation*, ed. SW Hawking, W Israel, pp. 330–458. Cambridge, UK: Cambridge Univ. Press
- Thorne KS, Zytow AN. 1975. *Ap. J. Lett.* 199:L19–24
- Touma JR, Tremaine S, Kazandjian MV. 2009. *MNRAS* 394:1085–108
- Vasiliev E. 2014. *Class. Quantum Gravity* 31:244002
- Vasiliev E, Merritt D. 2013. *Ap. J.* 774:87
- Volonteri M. 2010. *Astron. Astrophys. Rev.* 18:279–315
- Volonteri M. 2012. *Science* 337:544
- Wang J, Merritt D. 2004. *Ap. J.* 600:149–61
- Wardle M, Yusef-Zadeh F. 1992. *Ap. J. Lett.* 387:L65–68
- Wegg C, Bode JN. 2011. *Ap. J. Lett.* 738:L8
- Will CM. 2008. *Ap. J. Lett.* 674:L25–28
- Young PJ. 1977. *Ap. J.* 217:287–95
- Yu Q, Madau P. 2007. *MNRAS* 379:1293–301
- Yu Q, Tremaine S. 2002. *MNRAS* 335:965–76
- Yu Q, Tremaine S. 2003. *Ap. J.* 599:1129–38
- Zhang F, Lu Y, Yu Q. 2010. *Ap. J.* 722:1744
- Zucker S, Alexander T, Gillessen S, Eisenhauer F, Genzel R. 2006. *Ap. J. Lett.* 639:L21–24



Contents

Galaxies, Globular Clusters, and Dark Matter <i>Kenneth C. Freeman</i>	1
Stellar Dynamics and Stellar Phenomena Near a Massive Black Hole <i>Tal Alexander</i>	17
Theoretical Challenges in Galaxy Formation <i>Thorsten Naab and Jeremiah P. Ostriker</i>	59
Observing Interstellar and Intergalactic Magnetic Fields <i>J.L. Han</i>	111
Stellar Model Chromospheres and Spectroscopic Diagnostics <i>Jeffrey L. Linsky</i>	159
Markov Chain Monte Carlo Methods for Bayesian Data Analysis in Astronomy <i>Sanjib Sharma</i>	213
Magnetars <i>Victoria M. Kaspi and Andrei M. Beloborodov</i>	261
Ultraluminous X-Ray Sources <i>Philip Kaaret, Hua Feng, and Timothy P. Roberts</i>	303
Small-Scale Challenges to the Λ CDM Paradigm <i>James S. Bullock and Michael Boylan-Kolchin</i>	343
The Circumgalactic Medium <i>Jason Tumlinson, Molly S. Peebles, and Jessica K. Werk</i>	389
How to Characterize Habitable Worlds and Signs of Life <i>Lisa Kaltenegger</i>	433

Indexes

Cumulative Index of Contributing Authors, Volumes 44–55	487
Cumulative Index of Article Titles, Volumes 44–55	490

Errata

An online log of corrections to *Annual Review of Astronomy and Astrophysics* articles may be found at <http://www.annualreviews.org/errata/astro>